A Review of Pnictogenides for Next-Generation Anode Materials for Sodium-Ion Batteries

Sion Ha [1], Junhee Kim [1], Dong Won Kim [1], Jun Min Suh [2] and Kyeong-Ho Kim [1,*]

[1] Department of Materials Science and Engineering, Pukyong National University, Busan 48513, Republic of Korea; hasion1321@pukyong.ac.kr (S.H.); 12sovo9@pukyong.ac.kr (J.K.); okak2000@pukyong.ac.kr (D.W.K.)

[2] Department of Mechanical Engineering, Massachusetts Institute of Technology, Cambridge, MA 02139, USA

[*] Correspondence: khkim213@pknu.ac.kr; Tel.: +82-51-629-6360

Abstract: With the growing market of secondary batteries for electric vehicles (EVs) and grid-scale energy storage systems (ESS), driven by environmental challenges, the commercialization of sodium-ion batteries (SIBs) has emerged to address the high price of lithium resources used in lithium-ion batteries (LIBs). However, achieving competitive energy densities of SIBs to LIBs remains challenging due to the absence of high-capacity anodes in SIBs such as the group-14 elements, Si or Ge, which are highly abundant in LIBs. This review presents potential candidates in metal pnictogenides as promising anode materials for SIBs to overcome the energy density bottleneck. The sodium-ion storage mechanisms and electrochemical performance across various compositions and intrinsic physical and chemical properties of pnictogenide have been summarized. By correlating these properties, strategic frameworks for designing advanced anode materials for next-generation SIBs were suggested. The trade-off relation in pnictogenides between the high specific capacities and the failure mechanism due to large volume expansion has been considered in this paper to address the current issues. This review covers several emerging strategies focused on improving both high reversible capacity and cycle stability.

Keywords: sodium ion batteries; anode materials; pnictogenides; nitrides; phosphides; antimonides

1. Introduction

Lithium-ion batteries (LIBs) have emerged as a crucial innovation, constituting an efficient energy storage system with electrical energy generated by clean energy sources. The growing market for batteries for electric vehicles (EVs) and grid-scale energy storage systems (ESSs) has led to an favorable perspective on LIBs [1]. However, numerous studies have consistently raised concerns over the increasing price and instability of LIBs driven by limited reserves of lithium (Li) resources, which are essential for the construction of LIBs [2,3].

To address the above-mentioned issue, numerous studies have focused on discovering alternative systems using alkali metals or alkaline earth metals to mitigate the high cost of Li resources, such as sodium-ion batteries (SIBs), potassium-ion batteries (PIBs), or multi-valence ion (e.g., Ca^{2+} or Mg^{2+}) battery systems, utilizing more cost-effective carrier ions [4–6]. Among these next-generation battery systems, SIBs are regarded as the most promising candidate for commercialization as the atomic radius and molar weight of Na^+

ions are similar to those of Li+ ions when compared to other alkali metals and alkaline earth metals. In addition to the cost effectiveness of using inexpensive Na-containing precursors rather than expensive Li precursors, there is another benefit to using SIBs. Unlike LIBs, which use an aluminum (Al) current collector for the anode side due to the formation of an Li-Al alloy phase, there is no Na-Al alloy phase formation issue in SIBs, which is an additional advantage [7,8].

The similarity in working principles and energy storage mechanisms between SIBs and LIBs is another major factor stimulating research into SIBs, and several studies have adopted commercially proven anode materials used in LIBs for SIB systems. Unfortunately, the most representative anode material, graphite, showed poor electrochemical activity in SIBs as the formation of binary Na–graphite intercalation compounds (GICs) is thermodynamically suppressed. In contrast to the formation of LiC_6 phases such as GIC in LIBs, sodium-ion storage through forming an NaC_6 phase was prohibited [9]. To discover the commercially available anode material in the SIB system, hard carbon materials with randomly arranged graphitic layers have been widely applied for SIB applications, driving continued efforts toward the first commercialized anode materials for SIBs. However, the hard carbon anode still faces significant challenges, including low initial coulombic efficiency (ICE), poor rate performance, and limited reversible capacity [10,11].

In the case of high-capacity anode materials for LIBs, group-14 elements, such as silicon (Si), germanium (Ge), and tin (Sn), can form Li-rich phases (e.g., $Li_{4.4}Si$, $Li_{4.4}Ge$, and $Li_{4.4}Sn$) [12], while Si and Ge cannot form Na-rich phases as anode materials for SIBs (Figure 1). In contrast to the high theoretical capacity of Si, i.e., 4200 mAh g⁻¹ with the formation of the $Li_{4.4}Si$ phase, Si can only form the NaSi phase, wherein Na is stored at a 1:1 molar ratio with Si, resulting in a theoretical capacity to 955 mAh g⁻¹ [13]. Likewise, Ge, in a group-14 element like Si, can also form the NaGe phase, exhibiting a theoretical capacity of 369 mAh g⁻¹. The promising candidates for anode materials in group 14, which demonstrate high theoretical capacities in LIBs, achieve about one-fourth of their capacities in SIBs, limiting their applications in high-capacity anodes for SIBs. While Sn can form a Na-rich phase of $Na_{3.75}Sn$, similar to the $Li_{4.4}Sn$ phase in LIBs, the molar weight of Sn is too large to exhibit high capacity behavior, leading to a theoretical capacity of 847 mAh g⁻¹ [14,15].
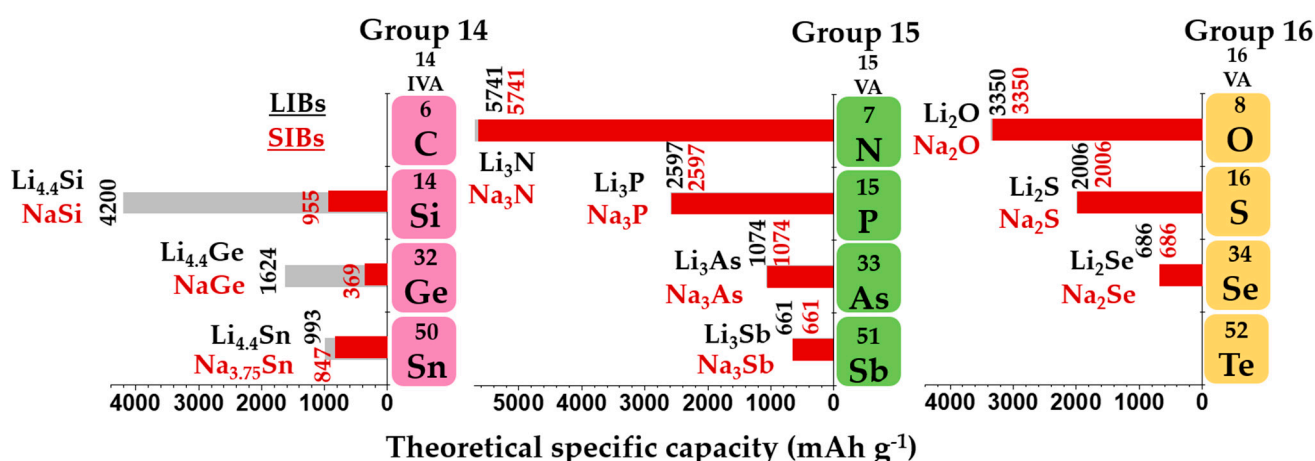

Figure 1. Theoretical capacities as anode materials for LIBs and SIBs in Group-14−16 elements.

On the other hand, chalcogens in group-16 elements, such as oxygen (O), sulfur (S), and selenium (Se), can form Na-rich phases of Na_2X (X = O, S, or Se), which allow for higher theoretical capacities than those of group-14 elements, exhibiting theoretical capacities of 3350 mAh g⁻¹, 2006 mAh g⁻¹, and 686 mAh g⁻¹ for Na_2O, Na_2S, and Na_2Se phases, respectively [15–17]. These values, while higher, are not dramatically large for high-

capacity materials. Additionally, the reaction potential of these chalcogens compared to Na/Na$^+$ is higher than those of group 14 and 15, leading to their lower practical energy densities [18,19]. In contrast, group-15 pnictogens, including nitrogen (N), phosphorus (P), arsenic (As), and antimony (Sb), provide a significant advantage in sodium-ion storage as they can store three Na ions per host (Na$_3$Y, Y = N, P, As, or Sb), resulting in a dramatic increase in theoretical capacity. In addition, the reaction potential of pnictogens with Na/Na$^+$ is considerably lower than that of other groups, indicating an advantageous feature for high-energy-density applications. P and Sb are the most widely studied elements in pnictogens, with high theoretical capacities of 2597 and 661 mAh g^{-1}, forming Na-rich phases of Na$_3$P and Na$_3$Sb, respectively [20–22]. In particular, N, with an atomic number of 7, forms a Na-rich Na$_3$N phase; while, at the same time, it has a lower molar weight, resulting in a much higher theoretical capacity of 5741 mAh g^{-1} among the other high-capacity candidates in anode materials for SIBs [23].

Therefore, in this study, based on the above-mentioned advantages of pnictogens for anode materials, our review highlights pnictogen-containing compounds of pnictogenides as promising candidates for attaining high energy density in SIBs. In the first part of this study, we introduce metal nitrides (MNs), which possess excellent electrical properties and offer higher theoretical capacities than other compounds. Despite compelling theoretical advantages, the studies on MNs as anodes for SIBs have not yet been systematically performed, providing an opportunity for further research [23,24]. In the second part of this study, metal phosphides (MPs), which have been the most intensively studied anodes for SIBs in pnictogenides, are summarized, with several compositions exhibiting high energy density performances. Both early and later transition metal (TM)-containing phosphides, as well as metal-rich and P-rich compounds, have been explored in order to understand their different electrochemical reaction mechanisms and properties [25,26]. Although As forms a Na-rich Na$_3$As phase with a theoretical capacity of 1072 mAh g^{-1}, and arsenide can be also applied to anode material applications, further research has not been undertaken due to the high toxicity and cost of As [27]. As-based pnictogenides show promising potential for energy storage applications, while they raise serious toxicity concerns, even for specific compositions like InAs, GaAs, and AlGaAs, which have been extensively studied and widely used in the semiconductor industry [28–30]. In the third part of this study, metal antimonides (MSbs) are introduced as they provide cost-effectiveness and environmental sustainability, with a relatively moderate reaction potential of about 0.4–0.8 V (vs. Na/Na$^+$) [31]. Despite the high theoretical capacities and lower reaction potentials of pnictogenides for SIBs, these materials encounter considerable challenges with low initial coulombic efficiencies (~80%) and severe volumetric changes during cycling, which results in poor cyclability [16,21,32,33]. The trade-off relation in pnictogenides between the high specific capacities and the failure mechanism due to large volume expansion has been considered to address these issues, and we introduce several emerging strategies focused on improving both high reversible capacity and cycle stability.

2. Physical and Chemical Properties of Pnictogenides

2.1. Metal Nitrides

MNs are advanced materials with exceptional physical, chemical, and electronic properties, making them highly promising for various technological applications. These compounds can exhibit metallic, ionic, or covalent bonding characteristics depending on their chemical composition and crystal structure, resulting in unique physical and chemical properties [34]. This structural arrangement modifies the lattice, causing d-band contraction and an increased density of states (DOS) near the Fermi level [35,36]. Such alterations impart noble-metal-like behavior and excellent electrical conductivity. MNs such

as VN and TiN exhibit outstanding electrical conductivities of 3.70×10^6 S m^{-1}, while NbN (1.60×10^6 S m^{-1}) and Mo$_2$N (2.97×10^4 S m^{-1}) also demonstrate significant conductivity, making them highly suitable for applications requiring efficient charge transport (Table 1).

MNs are also notable for their high density, as seen in materials like WN (17.7 g/cm^3), NbN (8.47 g/cm^3), and MoN (9.46 g/cm^3), which allows them to achieve superior volumetric energy densities compared to carbon-based materials. Their exceptional mechanical properties, including high Young's modulus values (e.g., NbN: 360 GPa and WN: 430 GPa), enhance their durability and stability under extreme conditions [37]. Despite these advantages, the practical application of MNs in electrochemical energy storage (EES) devices, such as lithium-ion batteries (LIBs), sodium-ion batteries (SIBs), lithium-ion hybrid capacitors (LiHCs), and supercapacitors (SCs), has been hindered by challenges such as brittleness, limited active sites, and compromised capacitance. However, recent advancements in MN composites have significantly addressed these issues by improving active sites, enhancing ion and electron transport, and increasing electrochemical stability [38,39].

Li$_3$N is a unique alkali nitride that stands out due to its exceptional ionic and structural properties. With a hexagonal α-phase structure under ambient conditions, Li$_3$N exhibits remarkable Li ion mobility and an ionic conductivity of 5.02×10^{-1} mS cm^{-1}. Its robust properties, such as a Young's modulus of 48 GPa and an indirect bandgap of 2.1 eV, further enhance its potential applications [38]. In contrast, Na$_3$N, another alkali nitride, remains poorly understood, and the role of the Na$_3$N phase in contributing to Na-ion storage capacity has not yet been clearly established as no definitive studies have explored its application in SIBs. This lack of clarity highlights the need for further research to determine its feasibility and effectiveness in SIB systems.

Table 1. Physical and chemical properties of metal nitrides with previously studied compositions as anode material for SIBs. Reproduced with permission [37]. Copyright 2021, Elsevier Ltd.

Materials	Crystal Structure	Density (g cm^{-3})	Electrical Conductivity (S m^{-1})	Young's Modulus (GPa)	Bandgap (eV)	Ref.
Mo$_2$N	Cubic	9.46	2.97×10^4	365	-	[35]
TiN	Cubic	5.40	3.70×10^6	281	3.4	[35]
VN	Cubic	6.13	3.70×10^6	344	Weak metallic	[40]
CoN	Cubic	6.18	-	485	Metallic	[41]
Ni$_3$N	Hexagonal	7.66	-	399	Metallic	[42]

2.2. Metal Phosphides

MPs, combining TMs and P, have garnered significant attention as cost-effective and easily synthesizable materials, positioning them as excellent candidates for a wide range of applications [25,43,44]. MPs have been extensively studied as energy storage materials due to their remarkable properties and adaptability. MPs are distinguished by their exceptional physical, chemical, and structural characteristics, which make them indispensable in energy storage, catalysis, and electronic applications. Their unique covalent–ionic hybrid bonding provides remarkable thermal and chemical stability. Depending on stoichiometry, MPs exhibit electronic behavior ranging from metallic to semiconducting. MPs, as exemplified by the Ni-P system, exhibit a wide range of intermediate compounds, including Ni-rich phosphides (Ni$_3$P, Ni$_5$P$_2$, Ni$_{12}$P$_5$, Ni$_2$P, and Ni$_5$P$_4$), mono-phosphide (NiP), and P-rich phosphides (NiP$_2$ and NiP$_3$), all characterized by diverse crystal structures [45]. Metal-rich MPs, such as Mo$_3$P and Co$_2$P, etc., characterized by extensive electron delocalization, show a high electrical conductivity that decreases electrical resistance during the cycling process in energy storage systems [46,47]. In contrast, P-rich MPs, such as CrP$_4$, MnP$_4$, FeP$_4$, and CoP$_4$, exhibit semi-metallic or semi-conducting behavior depending on their local arrangements of MP$_6$ octahedra and the corresponding electronic

structures (Figure 2). The electrical resistivity of MPs varies widely, ranging from a highly conductive phase of cubic (c)-NiP_2 (9 mΩ·cm) to an insulating phase of ZnP_2 (3×10^{10} mΩ·cm), with an intermediate example of monoclinic (m)-NiP_2 (390 mΩ·cm) phase. This broad range of resistivity enables MPs to function effectively in both conductive and insulating roles. MPs are produced using various synthesis techniques, such as solvothermal, ball milling, and gas–solid reactions, with hybridized orbitals like sp^3d^4 and sp^2d^5 contributing to their bonding strength and structural stability [48]. These various properties establish MPs as a potential key in materials science, with significant focus in energy storage materials, electrochemical catalysts, and thermoelectric materials [49–51].
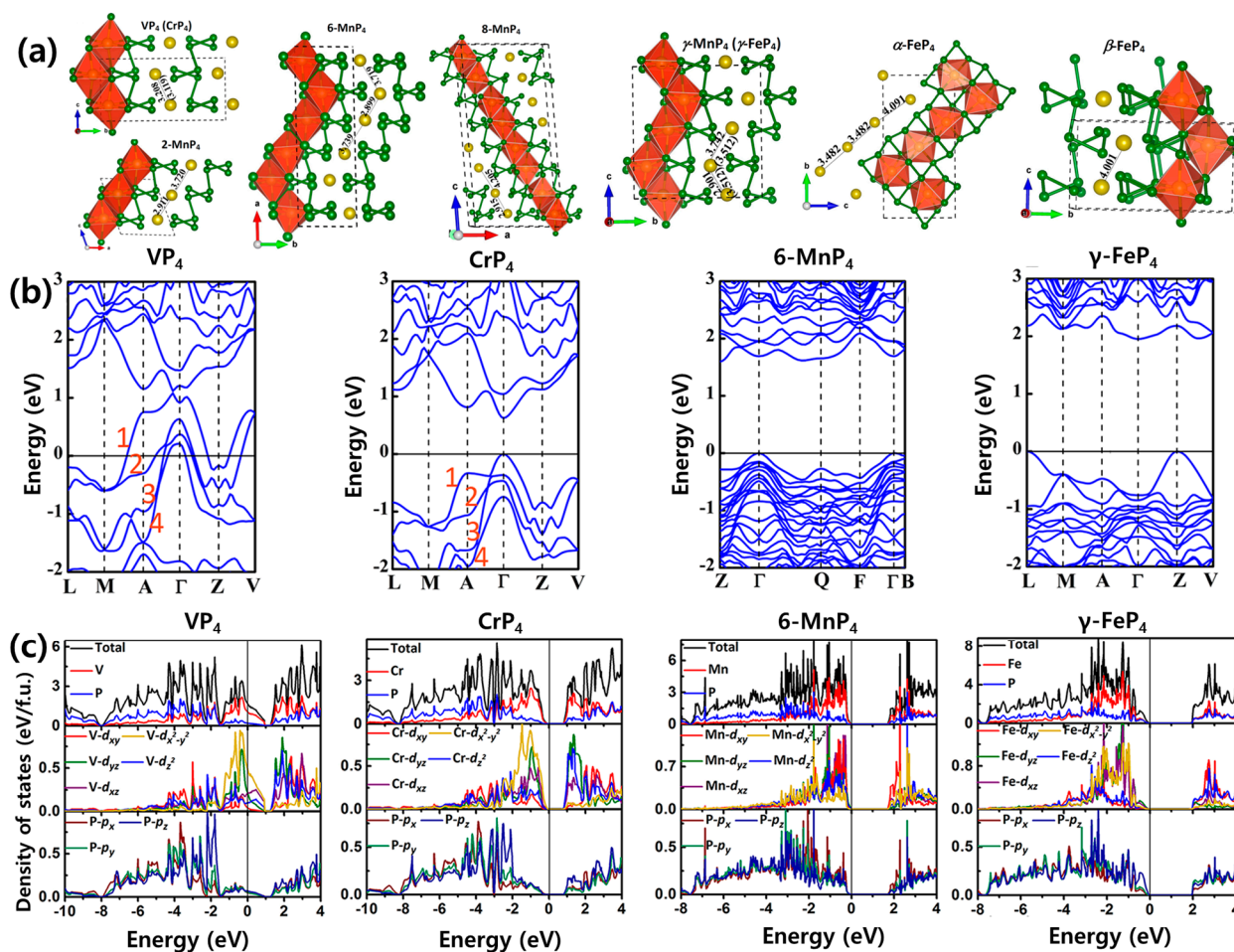
Figure 2. (**a**) Crystal structures, (**b**) calculated band structures, and (**c**) the corresponding total and partial density of states for transition metal tetraphosphides (TMP₄, TM = V, Cr, Mn, and Fe), respectively. Reproduced with permission [52]. Copyright 2018, American Chemical Society.

2.3. Metal Antimonides

First, before their adoption as energy storage materials, Sb-based metal compounds emerged as critical materials in semiconductor research, offering a unique combination of narrow bandgaps, high electron mobility, and stable crystal structures [53,54]. These properties render them indispensable for advanced technologies such as infrared sensors, high-speed electronic devices, and optical systems. The compositional flexibility of these materials, composed of group-13 elements (e.g., Ga, In, Al) and group-15 elements (e.g., Sb, As), allows for the precise tailoring of their electronic and optical properties. Key examples include GaSb, InSb, AlGaSb, and InAsSb, all of which are part of the "6.1 Å III-V family", named for their stable lattice constant of 6.1 Å. Despite these advantages, Sb-based compounds face certain limitations in specific applications [55].

For instance, InSb, with its narrow bandgap of 0.18 eV and remarkable electron mobility of 8×10^4 cm^2 V^{-1} S^{-1}, demonstrates excellent performance in infrared detection and high-speed electronic devices. However, its low thermal conductivity (0.15 W cm^{-1} K^{-1}) limits its usability in high-temperature environments. In contrast, GaSb features a relatively wider bandgap of 0.7 eV and an electron mobility of 1×10^3 cm^2 V^{-1} S^{-1}, combined with a low melting point of 712 °C, which provides thermal stability and ease of manufacturability. FeSb, on the other hand, has a very narrow bandgap of 0.1 eV and low electron mobility of 20 cm^2 V^{-1} S^{-1} but offers high mechanical stability, with a Mohs hardness of 4.5, ensuring durability under repetitive stress conditions [56]. These contrasting properties highlight the need for careful material selection based on specific application requirements.

From a chemical perspective, Sb-based compounds are highly advantageous due to their low formation energy and electrochemical stability, which simplify synthesis and facilitate material optimization [57]. SnSb exemplifies these traits with its excellent stability (-31 kJ mol^{-1}) and high theoretical capacity (847 mAh g^{-1}), maintaining superior performance during repeated charge–discharge cycles. Conversely, LaSb demonstrates considerable drawbacks, including its extremely low formation energy (-290 kJ mol^{-1}) and electrochemically non-reactive element of La, limiting its practical capacity. The reversible capacity of LaSb electrode is only limited to 114 mAh g^{-1}, achieving only 37% of the theoretical capacity, which emphasizes the disparities in performance among these materials [56]. As a result, antimonide-based compounds have the potential to expand their significance beyond their traditional role in semiconductor research. This is attributed to the ease of material designs, leveraging the theoretically predicted physical and chemical properties from previous studies for semiconductors and enabling the development of novel anode materials with various compositions and structures for SIBs.

3. Pnictogenides as Anode Materials for Sodium-Ion Batteries

3.1. Metal Nitrides as Anode Materials

Modern bonding theories with respect to MNs emphasize the strong binding energies between TMs and N atoms, which contribute to their structural and electrochemical stability. MNs are particularly advantageous for developing mechanically stable solid electrolyte interface (SEI) layers with high ionic conductivity (e.g., Li$_3$N phase) [39]. Compared to oxygen-based materials like TM oxides (TMOs), N anionic centers offer superior structural stability and faster alkali-ion diffusion kinetics, making them promising candidates for next-generation anode materials. MNs with chemical compositions of Ca$_2$N, TiN, VN, Mo$_2$N, MnN, Fe$_2$N, Fe$_3$N, Ni$_3$N, Cu$_3$N, and Sn$_3$N$_4$ have demonstrated significant potential in sodium-ion batteries (SIBs), combining robust structural properties with advanced electrochemical performance [58]. Beyond their catalytic and mechanical applications, MNs are now recognized for their high electronic conductivity and ability to handle substantial volume changes during sodiation and desodiation processes. These attributes address key limitations of chemistry in SIBs, positioning MNs as highly effective materials for future energy storage systems.

3.1.1. Metal-Rich Nitrides (M_aN_b, $a > b$)

In the Ni-N binary system, a variety of chemical compositions of compounds such as Ni$_4$N, Ni$_3$N, Ni$_2$N, Ni$_3$N$_2$, and NiN$_6$ can be theoretically synthesized [59]. However, the structural stability of Ni$_4$N, Ni$_3$N$_2$, and NiN$_6$ remains uncertain, and no research has yet demonstrated their application as anode materials for secondary batteries. Among the compounds with experimentally synthesized and in-depth studied metal-rich nitrides, trinickel nitride (Ni$_3$N) has been investigated by Hector et al. and found to be a promising

anode material for SIBs due to its stable electrochemical performance and high coulombic efficiency after initial cycles [60]. Ni_3N exhibits a hexagonal crystal structure (with a space group $P6_322$), and the electrochemical reaction of Ni_3N with Na ions was characterized by a conversion mechanism: $Ni_3N + 3\ Na^+ + 3\ e^- \rightarrow 3\ Ni^0 + Na_3N$. This reaction results in the formation of metallic nickel ($3\ Ni^0$) and sodium nitride (Na_3N) phases during the electrochemical reduction process. The abundant metallic nickel phases in the $3\ Ni^0/Na_3N$ composite generated can significantly enhance the electronic conductivity of the composite, facilitating charge transfer. X-Ray diffraction studies have indicated that during cycling, the Ni_3N structure is partially retained, with amorphous metallic phases dominating after prolonged cycling. Electrochemical testing revealed an initial sodiation capacity of 517 mAh g^{-1} at a rate of 0.1 C (1 C = 423 mA g^{-1}), with a corresponding desodiation capacity of 227 mAh g^{-1} at a low ICE of 44%. After 20 cycles, the reversible capacities reached 134 mAh g^{-1}, demonstrating ~60% cycle retention properties, requiring further studies applying carbon-based composite materials.

Ma et al. performed a study demonstrating that the core–shell structure of Fe_3N@C nanoparticles anchored on nitrogen-doped 3D carbon foam (3DNCF) is effectively applied to anode materials for SIBs, with notable advancements in cycling stability, rate performance, and capacity retention [61,62]. This material uses a melamine-based synthesis method, which involves immersing a precursor sponge in a solution of $Fe(NO_3)_3$, urea, and glucose, followed by thermal treatment at 700 °C under an argon atmosphere. The resulting Fe_3N@C/3DNCF composites contained approximately 27.5 wt.% of the Fe_3N phase. SEM and TEM images showed uniformly distributed Fe_3N nanoparticles, with an orthorhombic structure (80–100 nm) encapsulated by a 6–15 nm thick carbon layer, which effectively prevents the agglomeration of particles and enhances structural durability. The electrochemical Na ion storage/extraction mechanism is a reversible conversion reaction ($Fe_3N + 3\ Na^+ + 3\ e^- \leftrightarrow 3\ Fe^0 + Na_3N$), as validated via ex situ XRD analysis. The electrochemical performance of Fe_3N@C/3DNCF showed an initial reversible capacity of 536.1 mAh g^{-1}, with a low ICE of 56.4%. Over 2000 cycles at a high current density of 1 A g^{-1}, the material retained a reversible capacity of 374.8 mAh g^{-1}, with a high cycle retention of 95.1%. In particular, Fe_3N@C/3DNCF demonstrated excellent rate capabilities, delivering reversible capacities of 509.4, 455.5, and 260.9 mAh g^{-1} at current densities of 0.2, 0.5, and 5 A g^{-1}, respectively. The robust electrochemical properties and scalable synthesis approach make Fe_3N@C/3DNCF a compelling candidate for advancing SIB technology.

Chen et al. investigated the application of Ca_2N, a unique two-dimensional (2D) multilayered structure (Figure 3a), as a promising anode material for SIBs [61]. The distinctive structure of Ca_2N consists of N atoms positioned between layers of calcium (Ca), with free electrons localized within the interlayer spaces. This arrangement provides exceptional electrical conductivity and supports efficient Na ion insertion/extraction. The substantial interlayer spacing of the Ca_2N phase, i.e., 0.633 nm (significantly larger than the 0.37 nm of graphite), facilitates enhanced Na ion storage and diffusion in the structure. To address the sensitivity to moisture and air of the Ca_2N phase, a compression molding method was employed to embed Ca_2N powder into nickel foam, effectively maintaining its structural integrity. As shown in Figure 3b, the crystal structure of the Ca_2N phase is a rhombohedral structure with a space group of R-3m, with a prominent XRD reflection corresponding to the (003) plane. The Ca_2N electrode showed an impressive initial discharge capacity of 1110.5 mAh g^{-1}, while only a low reversible capacity of 320 mAh g^{-1} was obtained at a current density of 50 mA g^{-1}, with a poor ICE of 28.8% (Figure 3c). Rate capability tests revealed discharge capacities of 343, 244, and 131 mAh g^{-1} at different current densities of 50, 200, and 2000 mA g^{-1}, respectively (Figure 3d). Although this material shows a large initial discharge capacity, further studies are required to address the significantly poor ICE and to achieve the improved reversible capacity.
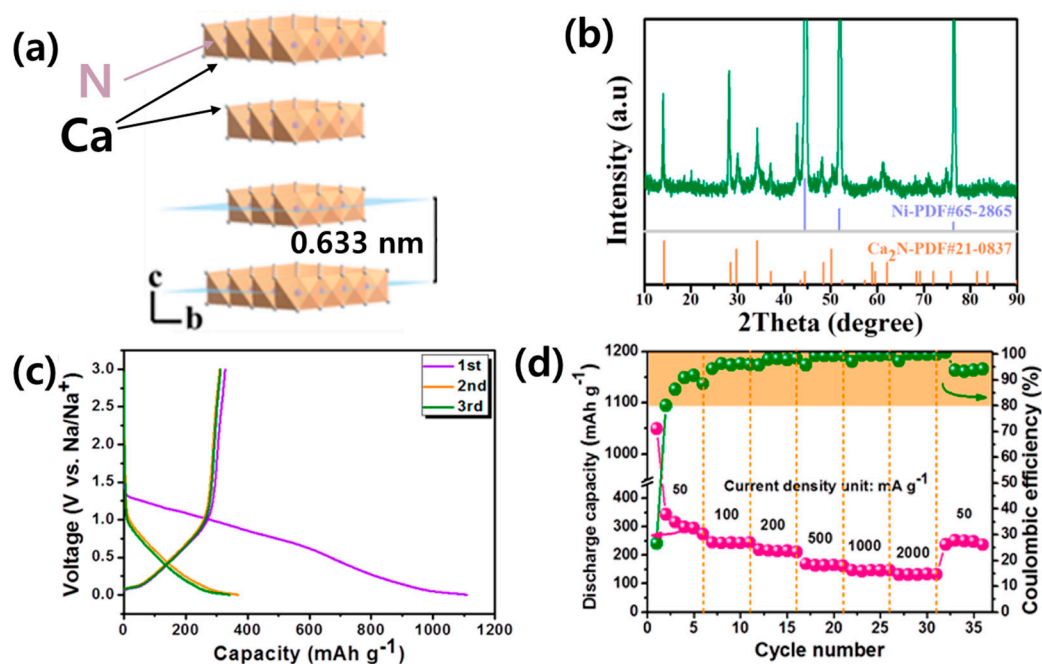
Figure 3. (**a**) Crystal structures, (**b**) XRD patterns, (**c**) voltage profiles at a current density of 50 mA g^{-1}, and (**d**) rate capability tests at different current densities of Ca$_2$N, respectively. Reproduced with permission [61]. Copyright 2017, American Chemical Society.

Molybdenum nitride (Mo$_2$N) nanoparticles encapsulated in carbon layers and anchored on reduced graphene oxide (Mo$_2$N@C-rGO) were extensively studied by Park et al. as a potential high-performance material for SIBs [63]. Employing a rapid and scalable microwave-assisted synthesis method produces Mo$_2$N nanoparticles with a crystallite size of 0.25 nm, encapsulated within 14–22 layers of carbon and distributed uniformly on the graphene substrate. Electrochemical characterization demonstrated the remarkable performance of this material, exhibiting an initial discharge capacity of 1049.6 mAh g^{-1} and a charge capacity of 441.2 mAh g^{-1} at a high current density of 500 mA g^{-1}. In addition, the composite electrode well retained a reversible capacity of 487.2 mAh g^{-1} after 50 cycles at a current density of 200 mA g^{-1}. This stable performance was attributed to the synergistic effects of alloying reactions between Na ions and Mo$_2$N and the intercalation of Na ions into the carbon shells and graphene layers simultaneously.

3.1.2. Metal Mono-Nitrides (M$_a$N$_b$, a = b)

Metal mono-nitrides, particularly those with a 1:1 molar ratio of M to N, have emerged as promising candidates for SIB applications. In particular, focusing on VN, MNs have gained attention as alternatives to layered carbon-based materials for electrochemical energy storage.

Xu's research team fabricated a vanadium nitride/carbon fiber (VN/CNF) composite using a versatile and scalable electrospinning method, widely employed for synthesizing 1D nanofibers and microfibers with various architectures, with an average diameter of 150 nm [64]. The carbon framework further played a crucial role in uniformly encapsulating active substances, effectively preventing aggregation, and improving material stability. Raman spectroscopy identified the D and G bands at 1329.3 cm^{-1} and 1588.3 cm^{-1}, confirming the presence of graphitized carbon and VN phases. This approach enabled the formation of nanofiber structures that established a conductive network, significantly enhancing electronic conductivity and providing rapid reaction kinetics. As a result, the composite showed an initial discharge capacity of 793 mAh g^{-1} at a current density of 100 mA g^{-1} and retained a reversible capacity of 403 mAh g^{-1} after 100 cycles. In addition, this

material showed excellent cycle stability, with a reversible capacity of 237 mAh g^{-1} at 2 A g^{-1} over 4000 cycles. The superior performance was attributed to the electrochemically reversible conversion reaction mechanism (VN + 3 Na$^+$ + 3 e$^-$ ↔ V + Na$_3$N) for Na ion storage and the robust conductive carbon nanofiber network.

　　　Meanwhile, a different approach was applied to modify the crystal structure of the VN phase to enable energy storage through intercalation reactions. Presented by the Song's team, VN anode materials were prepared by transforming the conventional bulk VN structure into a newly engineered layered configuration [65]. While conventional VN suffers from challenges such as substantial volume changes and limited cycling stability due to its conversion reaction mechanism, the layered VN presented here leverages an intercalation pseudocapacitive mechanism. This mechanism is facilitated by Al atoms positioned as structural pillars within the interlayer spacing, hindering the occurrence of conversion reactions. Intercalation pseudocapacitive-type VN was developed through a simple ammonification method, in which V2C MXene underwent treatment in an ammonia-rich atmosphere. As shown in Figure 4a, the introduced Al pillars stabilize the framework, enhancing its ability to accommodate Na ions while preserving structural integrity. Structural analysis techniques using XRD and TEM confirm the interlayer spacing of the VN structure as approximately 2.9 Å, enabling efficient ion transport and significantly improving electrochemical performance (Figure 4b). The layered VN delivers a high specific capacity of 280 mAh g^{-1} at 50 mA g^{-1} and exceptional cycling stability, retaining 115 mAh g^{-1} over 7500 cycles at 500 mA g^{-1} without capacity loss (Figure 4c). Mechanistic insights from in situ XRD and ex situ X-ray absorption spectroscopy (XAS) analysis reveal that the intercalation pseudo-capacitance mechanism underpins its outstanding performance. When VN was integrated with rGO (VN@rGO), its electrochemical performance significantly improved, achieving a capacity of 400 mAh g^{-1} at 50 mA g^{-1}. Additionally, the composite demonstrated excellent cycling stability, retaining 155 mAh g^{-1} after 10,000 cycles, even at a high current density of 1 A g^{-1} (Figure 4d). However, the ICE for both VN and VN@rGO remained extremely low, i.e., at around 12%. This issue is believed to stem from an electrolyte mismatch, underscoring the necessity of addressing this limitation through further research and optimization.
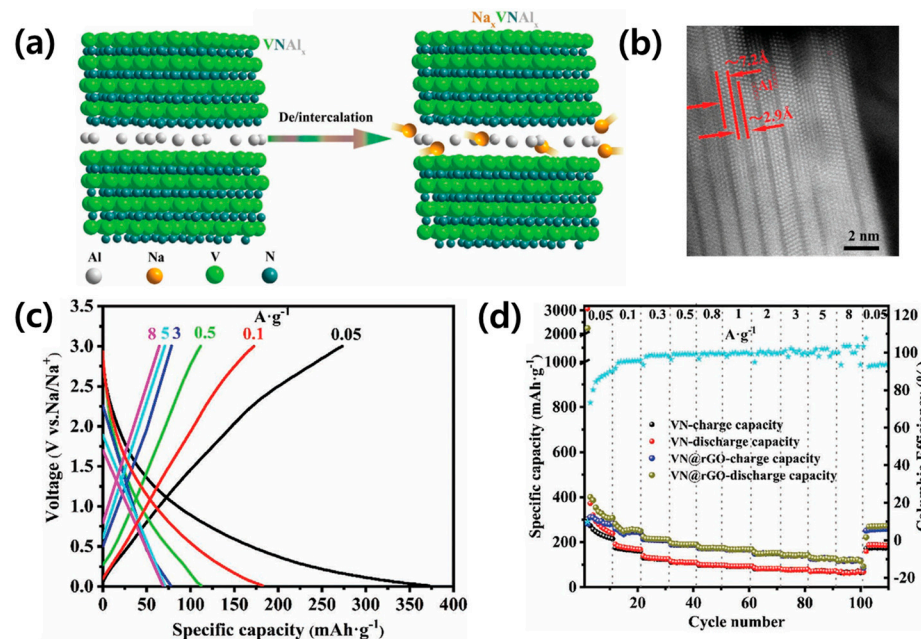
Figure 4. (**a**) Schematic illustration of de/intercalation mechanism for Al-atoms-pillared VN. (**b**) STEM image and (**c**) voltage profiles of VN at current density ranges from 50 to 8000 mA g^{-1}. (**d**)

Rate capabilities at different current densities of VN and VN@rGO, respectively. Reproduced with permission [65]. Copyright 2020, Wiley-VCH.

Manganese nitrides exhibit a variety of stoichiometries, including nitrogen-deficient phases, such as Mn_3N_2, Mn_5N_2, Mn_2N, and Mn_4N, and the mono-nitride of the MnN phase. These compounds have been widely explored, particularly for their intriguing magnetic properties. Park et al. show a development of MnN@rGO as an anode material for SIBs by preparing MnO_x precursors with hexamethylenetetramine (HMTA) under a nitrogen–ammonia atmosphere for the uniformly dispersed MnN nanoparticles (130–210 nm) on a mesoporous rGO framework (Figure 5a–c) [66]. With a high surface area of 521 m^2 g^{-1}, the rGO serves as a conductive matrix that mitigates volume expansion from MnN and enhances electron and ion transport during cycling. The high theoretical capacity of MnN is calculated as 1166 mAh g^{-1} based on the following conversion reaction, namely, MnN + 3 Na$^+$ + 3 e$^-$ → Mn^0 + Na$_3$N, but further study is required in order to define the detailed reaction mechanism. The MnN@rGO electrode achieves exceptional initial discharge and charge capacities of 1635.8 and 850.5 mAh g^{-1}, respectively, at a current density of 250 mA g^{-1} (Figure 5d). This corresponds to an ICE of 52.14%, which is typical for nitride anodes and might be due to the formation of a solid electrolyte interphase (SEI) during the first cycle. The composite electrode also exhibits a reversible capacity of 716 mAh g^{-1} after 180 cycles at 50 mA g^{-1} and maintains 240 mAh g^{-1} at 1 A g^{-1}, demonstrating excellent rate performance and cycling stability (Figure 5e). While this study successfully demonstrates scalability with the earth-abundant element of Mn and the superior performance of the MnN@rGO composite, further investigations into full-cell configurations and electrolyte optimization are recommended to improve practicality.
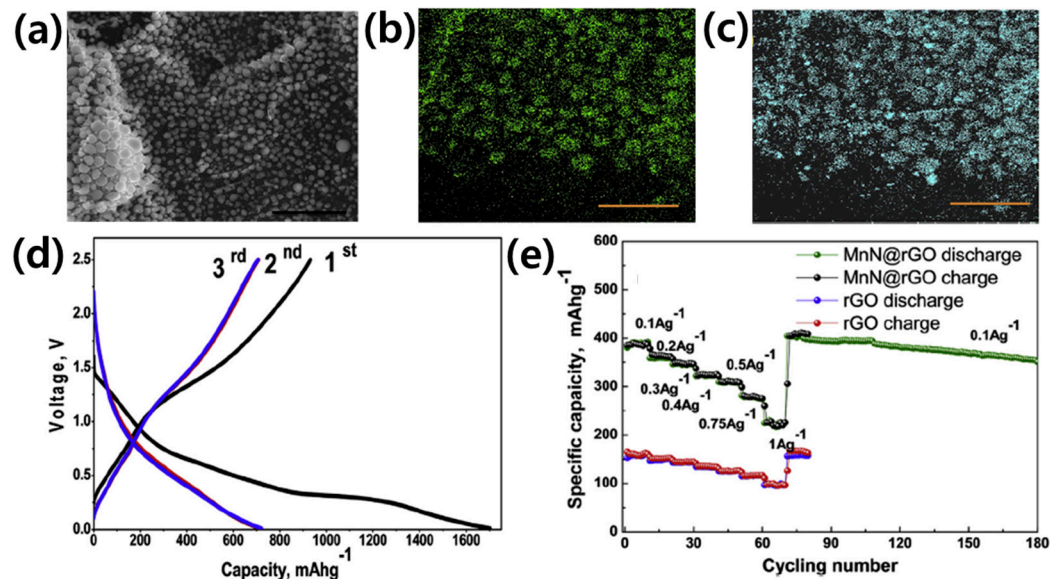
Figure 5. (**a**) In-lens image and EDS mapping images of (**b**) N K edge and (**c**) Mn K edge. (**d**) Voltage profiles and (**e**) rate capabilities of MnN@rGO at different current densities, respectively. Reproduced with permission [66]. Copyright 2019, Elsevier Ltd.

3.1.3. N-Rich Nitrides (M_aN_b, a < b)

In the case of Sn_3N_4, Fitch's team focused on both the electrochemical activities of Sn and N in the Sn_3N_4 phase, where Sn can alloy with Na ions at a molar ratio of 3.75:1 [67], and N can store up to few Na ions by forming some sort of Na-N compound, resulting in an exceptionally high theoretical capacity of 1512 mAh g^{-1} [68]. In particular, two sequential reactions were proposed via density functional theory (DFT) calculations and ex situ

XRD and XAS, involving the conversion of Sn_3N_4 into Sn and Na-N, followed by the alloying of Sn with Na to form $Na_{15}Sn_4$. However, further analytical studies on the formed Na-N phases, particularly on the formation of the Na-rich Na_3N phase, are necessary to clarify the underlying mechanism [62,65,69].

This research emphasizes a scalable solvothermal synthesis method that utilizes $SnCl_4$ and $LiNH_2$ precursors in benzene under mild conditions, producing Sn_3N_4 with a cubic spinel structure (space group of Fd-3m). Microcrystalline Sn_3N_4, synthesized at higher temperatures, exhibited crystallite sizes of 310 nm, while nanocrystalline Sn_3N_4, produced at lower temperatures with sonication, achieved smaller particle sizes of 5.95 nm, enhancing surface area and Na ion accessibility. This nanocrystalline Sn_3N_4 demonstrated remarkable electrochemical performance, achieving a reversible capacity of 850 mAh g^{-1} at 50 mA g^{-1}, with excellent cycling stability. Despite these advancements, challenges such as low ICE of 30~45%, incomplete utilization of theoretical capacity, and surface-related side reactions remain. The increased surface area of nanocrystalline Sn_3N_4, while enhancing capacity, also leads to irreversible capacity losses during initial cycles due to SEI formation and electrolyte decomposition. To address these issues, this study suggests optimizing electrolytes, exploring advanced nanostructures such as yolk–shell designs, and conducting full-cell evaluations. The strategy using MNs containing two elements that both react with Na ions, combined with the robust synthesis method, shows the potential of Sn_3N_4 as a high-capacity anode material for next-generation SIBs, paving the way for significant advancements in energy storage technologies.

### 3.2. Metal Phosphides as Anode Materials

MPs, i.e., compounds formed by the combination of P and M, have emerged as promising anode materials to overcome the challenges associated with P (especially red P), such as flammability, poor electrical conductivity, and significant volume expansion (>300%) issues. These compounds have gained the most notable attention in recent years for their use in SIBs due to their ability to retain the high-capacity characteristics of P while addressing its inherent limitations. Compared to other materials, such as metal oxides and sulfides, MPs exhibit lower reaction potentials with Na ions, resulting in them being highly suitable for high-energy-density applications. The Li ion storage mechanism of transition metal phosphides (TMPs) depends significantly on the type of TM used. As an example, in the mono-phosphide group, early TM-containing TiP, VP, and MoP possess the large ionic radii of TM and facilitate the creation of prismatic sites for Li ion insertion/extraction. Moreover, the relatively low electronegativity of these early TMs ensures that their crystal structure remains intact during lithiation near the Li/Li$^+$ reduction potential as they do not undergo a complete reduction process for electrochemical conversion reactions. These two features mainly contribute to demonstrating the topotactic insertion/extraction mechanism with Li ions for early TMPs. In contrast, MnP, containing middle TM of Mn, stores Li ions through an alloying reaction mechanism rather than a topotactic insertion mechanism, and later, TM, containing FeP, CoP, and NiP, undergoes an electrochemical conversion reaction via the same correlation in terms of ionic radius and the electronegativity of TMs (i.e., later TMs can easily be reduced to their metallic state and underwent a conversion reaction mechanism). However, most previously reported MPs exhibit an electrochemical conversion reaction mechanism near the Na/Na$^+$ reduction potential, with one exception to the topotactic insertion/extraction reaction mechanism observed in the V_4P_7 phase [70]. In addition, the electrochemically active composition of MnP, VP_2, and FeP_2, etc., in LIBs indicates less activity in SIB applications [71]. In the case of P-rich MPs, their electrochemical performances exhibit highly promising anode materials for SIBs due to their exceptionally high specific capacity and low operating potentials (ranging from 0.3 to 0.7 V vs. Na/Na$^+$), such as in the case of NiP_3, MnP_4, and CrP_4 [72–74].

However, in P-rich MPs, the severe capacity degradation caused by significant volume expansion is a critical issue, necessitating further research for further improvement. These unique properties make MPs a compelling choice for advancing SIB technology, with specific advantages and limitations for each type of MP [47].

3.2.1. Metal-Rich Phosphides (M_aP_b, a > b)

Yu et al. introduced hollow-structure Cu_3P as a promising anode material for SIBs, synthesizing Cu-rich phosphide through a simple one-step phosphorization process. In the Cu-P binary system, the Cu_3P, CuP_2, and Cu_2P_7 phases are potential candidates to be synthesized. Among them, Cu_3P, as a metal-rich phase, exhibits the highest electrical conductivity [75,76]. Additionally, its abundant Cu matrix may provide the advantage of suppressing volume expansion during the P redox reactions that occur during the formation of Na_3P, ensuring better structural stability. The synthesis process involved the reaction of CuO precursors with red phosphorus in an argon atmosphere, resulting in hollow particles, with sizes below 500 nm, formed via the nanoscale Kirkendall effect. During sodiation, Cu_3P undergoes a conversion reaction whereby Cu_3P reacts with Na ions to form metallic copper (Cu^0) and the Na_3P phase, with the hollow structure accommodating the significant volume expansion (~156%) associated with this process. Electrochemical evaluations demonstrated a reversible capacity of 159.0 mAh g^{-1}, with an ICE of 53.7%, which improved to 97.8% after a few cycles. The hollow structure effectively accommodated the significant volume expansion during sodiation, while the conductive Cu framework minimizing polarization, ensuring excellent cycling stability and rate performance. Full-cell tests with a P2-$Na_{2/3}Ni_{1/3}Mn_{1/2}Ti_{1/6}O_2$ cathode achieved an energy density of 189.3 Wh kg^{-1} and an average discharge voltage of 2.91 V, with a capacity retention of 56.3% over 20 cycles. This work highlights the potential of Cu_3P as a next-generation SIB anode material, with further improvements in ICE and long-term stability required to fully realize its practical applicability.

Ni-containing metal-rich phosphides have been also extensively studied, and Wang et al. introduced the Ni_2P phase as an anode for SIBs [77]. In this study, using a stepwise synthesis process, NiS_2 solid octahedrons were transformed into hollow Ni_2P particles through phosphorization (Figure 6a), followed by carbon coating. TEM and HRTEM images clearly show a yolk–shell structure with a Ni_2P core and a carbon shell separated by a void (Figure 6b,c). The XRD pattern confirmed that Ni_2P adopts an orthorhombic structure (the space group of Pnma), and the sodium storage mechanism involves a conversion reaction ($Ni_2P + 3\ Na^+ + 3\ e^- \leftrightarrow 2\ Ni^0 + Na_3P$), achieving a theoretical capacity of 542 mAh g^{-1} (Figure 6d). The carbon shell enhances electrical conductivity, and the void space mitigates the applied mechanical stress during Na_3P formation. For SIBs, electrochemical testing showed that Ni_2P/C achieved an initial discharge capacity of 464 mAh g^{-1} at 100 mA g^{-1}, with an ICE of 67.5%. The cycle performance of this material exhibits a reversible capacity of 291.9 mAh g^{-1} after 300 cycles at 100 mA g^{-1} (Figure 6e). The yolk–shell design provides exceptional structural stability by accommodating significant volume changes and maintaining electrode integrity.
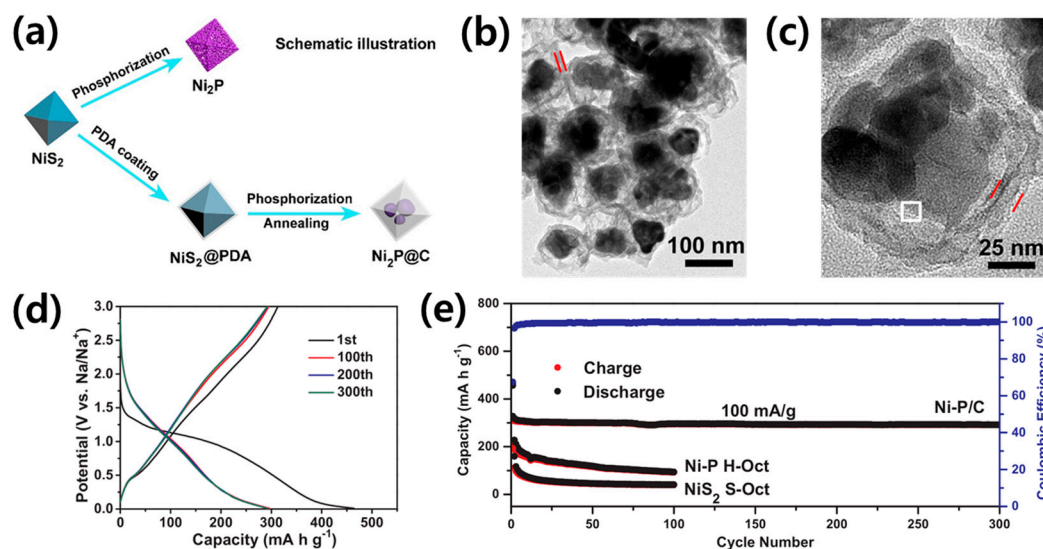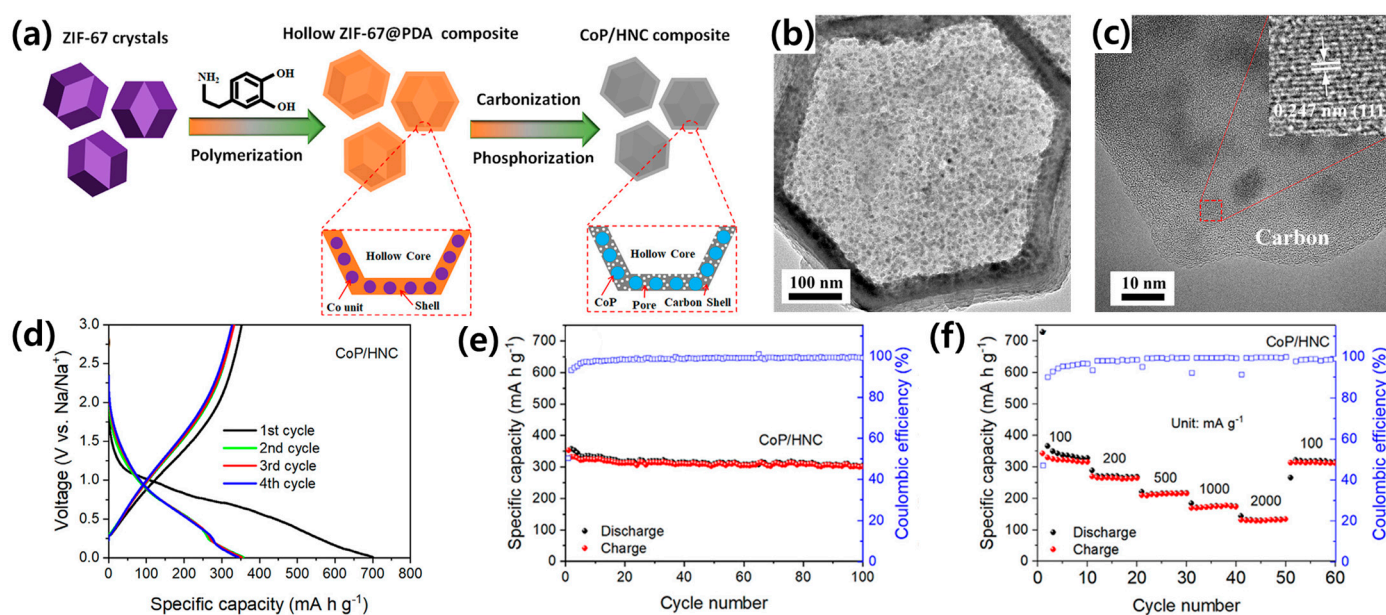
Figure 6. (**a**) Schematic illustration of the formation of the Ni$_2$P H-Oct and Ni$_2$P@C yolk–shell nanocomposite. (**b**) Low- and (**c**) high-magnification TEM images and (**d**) voltage profiles at a current density of 100 mA g^{-1} of the Ni$_2$P@C nanocomposite, respectively. (**e**) Cycle performances of NiS$_2$ S-Oct, Ni$_2$P H-Oct, and Ni$_2$P@C nanocomposite at a current density of 100 mA g^{-1}. Reproduced with permission [77]. Copyright 2019, Elsevier Ltd.

3.2.2. Metal Mono-Phosphides (M$_a$P$_b$, a = b)

As part of the broader metal mono-phosphide family, FeP stands out for its potential to address the challenges of energy storage, leveraging the high theoretical capacities and unique properties associated with TMPs, which utilize Fe, a metal abundantly found in the Earth's crust. FeP has established itself as a promising candidate for high-capacity anode materials in SIBs due to its superior electrical conductivity compared to iron oxides. FeP employs a conversion reaction mechanism, and its practical application is hindered by significant volume expansion during cycling, which can lead to structural instability and capacity degradation. To overcome these limitations, Alamgir et al. studied porous FeP/C composite nanofibers (NFs) as a mitigating strategy regarding the severe volume expansion of the material through a multistep synthesis process combining electrospinning, carbonization, oxidation, and phosphidation [78]. The resulting FeP/C NFs exhibit a porous architecture, with FeP nanoparticles being well dispersed in a conductive CNF matrix. These structural advantages enable remarkable electrochemical performance for SIBs, providing efficient pathways for ion transport and buffering volume changes during cycling. The Na ion storage mechanism involves a two-step process, combining the first intercalation reaction (FeP + x Na$^+$ + x e$^-$ ↔ Na$_x$FeP) and the following conversion reaction, forming Na$_3$P and metallic Fe^0. As a result, FeP/C NFs exhibit an initial discharge capacity of 530 mAh g^{-1} at 200 mA g^{-1}, showing an ICE of 69.8%. Over 300 cycles, a reversible capacity was found to be 531 mAh g^{-1} at 200 mA g^{-1}, resulting in a capacity retention of 99.9%. The composite significantly outperformed bare FeP, underscoring the importance of its porous carbon framework in addressing conductivity and mechanical challenges.

In the case of CoP, unlike FeP, which utilizes both intercalation and conversion reactions, CoP relies solely on a conversion reaction mechanism whereby the Co–P bonds break to form metallic Co^0 and Na$_3$P. Si et al. developed a CoP composite encapsulated within hollow nitrogen-doped carbon (CoP/HNC) shells, which provides Na ion diffusion pathways (Figure 7a) [79]. CoP/HNC was synthesized via a multi-step process involving ZIF-67 crystal polymerization, carbonization, and phosphorization. As shown in the images of TEM and HRTEM, this unique structure integrates monodisperse CoP

nanoparticles (~10 ± 2 nm) into a hollow nitrogen-doped carbon framework (Figure 7b,c). CoP/HNC electrodes exhibit an initial reversible capacity of 353.3 mAh g^{-1} at 100 mA g^{-1}, with a relatively low ICE of 50.4% (Figure 7d), and CoP/HNC retains a capacity of 223 mAh g^{-1} after 700 cycles, with a 95.7% capacity retention under high current density conditions (at 500 mA g^{-1}) (Figure 7e). In addition, Figure 7f shows the good rate capability of CoP/HNC, delivering a reversible capacity of 133 mAh g^{-1} at 2.0 A g^{-1}. Combining a conversion reaction of CoP nanoparticles (CoP + 3Na$^+$ + 3e$^-$ ↔ Co + Na$_3$P) and an insertion reaction with the conductive nitrogen-doped carbon matrix, CoP/HNC composite ensures enhanced stability, abundant active sites, and efficient ion/electron transport, highlighting the long lifespan potential at a high current density for SIBs.

Figure 7. (**a**) Schematic illustration of synthesis process, (**b**) low- and (**c**) high-magnification TEM images, (**d**) voltage profiles, (**e**) cycle performance at a current density of 100 mA g^{-1}, and (**f**) rate capabilities at different current densities of the CoP/HNC composite, respectively. Reproduced with permission [79]. Copyright 2021, Elsevier Ltd.

3.2.3. P-Rich Phosphides (M$_a$P$_b$, a < b)

Kim et al. successfully synthesized V$_4$P$_7$ nanoparticles, and this unique P-rich compound possesses a topotactic Na ion insertion/extraction mechanism near the Na/Na$^+$ reduction potential based on the unique tetragonal crystal structure (space group of P-4m2, Figure 8a) [70]. With a distinct low sodiation plateau around 0.1 V (vs. Na/Na$^+$), the initial discharge and charge capacities were 343 and 240 mAh g^{-1} at 50 mA g^{-1}, respectively (Figure 8b). Notably, ex situ XRD, TEM, and XAS analyses confirmed that the V$_4$P$_7$ phase remained intact, with no observable phase changes or amorphization during the sodiation/desodiation processes, even after electrochemical testing, indicating a reversible insertion/extraction mechanism (Figure 8c–e). In particular, the V$_4$P$_7$ electrode exhibited an excellent cycle retention of 99.99% after 100 cycles at 100 mA g^{-1}, delivering a discharge capacity of 234 mA h g^{-1} without any conductive coatings or agents. Additionally, a long-term cycling test at 500 mA g^{-1} demonstrated that a reversible capacity of 122 mAh g^{-1} was achieved in the V$_4$P$_7$ electrode, with a 96% retention over 500 cycles, exhibiting its reversible cyclability even at a high current density (Figure 8f). The remarkable durability of the electrode is attributed to its topotactic Na ion insertion/extraction mechanism, ensuring structural stability and fast ion diffusions throughout the crystal structure of the V$_4$P$_7$ phase.
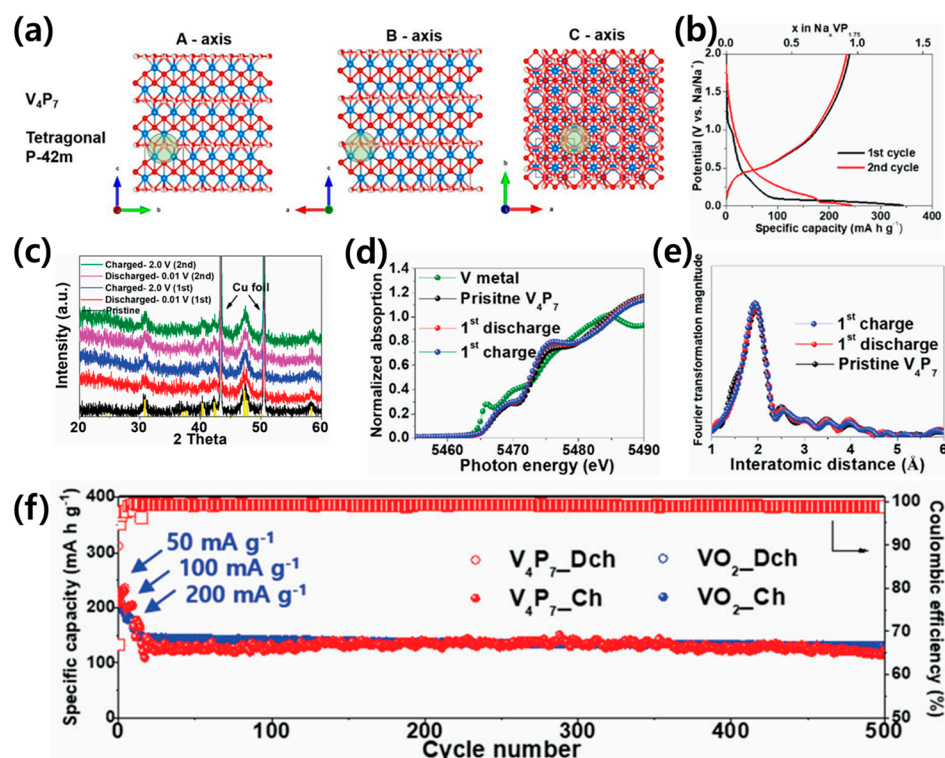
Figure 8. (**a**) Crystal structure and (**b**) ex situ voltage profiles at a current density of 50 mA g^{-1}. Ex-situ (**c**) XRD patterns, (**d**) XANES spectra, (**e**) EXAFS spectra, and (**f**) long-term cycling performance at a current density of 500 mA g^{-1} of V$_4$P$_7$, respectively. Reproduced with permission [70]. Copyright 2019, Royal Society of Chemistry.

Among the P-rich phosphides, metal polyphosphides (MP$_n$, n ≥ 2) have emerged as promising anode materials for SIBs due to their high theoretical capacities (over 1000 mAh g^{-1}) and suitable reduction potentials (0.1–0.9 V vs. Na/Na$^+$), making them advantageous compared to oxides and chalcogenides. However, despite their theoretical capacity, the practical capacities of MP$_2$ materials often fall short. This issue is largely attributed to their poor electrical conductivity and severe volume expansion during cycling, leading to capacity degradation, poor electrochemical stability, and the persistent formation of an unstable SEI layer [80].

Copper diphosphide (CuP$_2$), which forms the monoclinic structure (space group of P2$_1$/c), offers unique advantages within this class of materials, including natural abundance of Cu, high conductivity, and the ability to form conductive Cu networks during conversion reactions. Nonetheless, these benefits are offset by challenges such as structural instability and voltage hysteresis, necessitating innovative material designs. To solve this problem, Wu et al. developed graphene-encapsulated CuP$_2$ composites, combining CuP$_2$ particles with a graphene (G) network to enhance conductivity, buffer volume expansion, and improve cycling stability [81]. The CuP$_2$@G composite was synthesized via a two-step ball milling and graphene encapsulation process, producing submicron-sized CuP$_2$ particles uniformly coated with graphene layers (~3–5 nm thick). The electrochemical mechanism involves a reversible conversion reaction: CuP$_2$ + 6 Na$^+$ + 6 e$^-$ ↔ 2 Na$_3$P + Cu^0. The CuP$_2$@G composite demonstrated an initial discharge capacity of 780 mAh g^{-1} at 100 mA g^{-1}, showing a reversible capacity 460 mAh g^{-1} after 50 cycles at 100 mA g^{-1}, with a coulombic efficiency approaching 100%. At a high current density of 1 A g^{-1}, it retained 240 mAh g^{-1} after 500 cycles, and its rate capability remained competitive, achieving 320 mAh g^{-1} at 2 A g^{-1}. One of the reasons for this performance is the effect of graphene

encapsulation, which provides a conductive matrix to improve electron transport, buffering the volume changes associated with Na_3P formation, and preventing particle aggregation.

Kim et al. explored the performance of NiP_3@CNT composites as anode materials for SIBs as synthesized through a high-energy ball milling (HEBM) process [72]. Crystalline NiP_3 nanoparticles were synthesized via HEBM using Ni and red P powders for 50 h, followed by 5 h of milling with functionalized CNTs, ensuring uniform dispersion and chemical bonding. XPS spectra showed strong P–C and P–O–C bonds that enhanced mechanical and electrochemical stability due to a highly electric-conductive CNT matrix. A high initial reversible capacity was achieved, i.e., 821.1 mAh g^{-1} at 100 mA g^{-1}, maintaining a reversible capacity of 80% during 120 cycles. Furthermore, NiP_3@CNT showed excellent rate capabilities, delivering 493.6 mAh g^{-1} at a high current density of 3200 mA g^{-1}. During long cycling tests at a current density of 1600 mA g^{-1}, the electrode retained 65% of its initial reversible capacity after 200 cycles. Electrochemical impedance spectroscopy (EIS) revealed significantly reduced charge transfer resistance (R_{ct}), and the Na ion diffusion coefficient (D_{Na^+}) was two orders of magnitude higher in the NiP_3@CNT composite compared to that of pristine NiP_3. The robust CNT matrix effectively buffered the volume expansion during sodiation, maintaining structural integrity and ensuring stable cycling.

The MnP_4 phase is one of the most promising anode candidates containing the earth-abundant element of Mn in P-rich compositions among metal tetra-phosphides (such as FeP_4 and CrP_4). It was synthesized by Kim et al. using the HEBM process [73]. As shown in Figure 9a, in the as-synthesized triclinic structure of 6-MnP_4, a repeating zigzag arrangement is observed along the a-axis, formed by units of six MnP_6 octahedra sharing edges. Each manganese atom within the structure is octahedrally coordinated by six P atoms. To address the large volume change issues of P-rich phosphides occurring during cycling effectively, MnP_4/graphene composites (MnP_4/G20) were prepared by incorporating 20 wt.% of graphene nanosheets through an additional milling step. The as-prepared MnP_4 nanoparticles consisted of 5 to 20 nm sized nanocrystallites, while the graphene sheets were evenly distributed, forming a robust conductive network. The theoretical specific capacity of MnP_4 is calculated to be 1876 mAh g^{-1} for LIBs and SIBs based on the full conversion reaction: $MnP_4 + 12Na^+ + 12e^- \leftrightarrow Mn + 4Na_3P$. In fact, ex situ XRD analysis undertaken by Kim et al. reveals the formation of Na_3P phase after the first sodiation process (Figure 9b). The MnP_4 electrode delivered an initial discharge capacity of 1234 mAh g^{-1} and a charge capacity of 1028 mAh g^{-1}, resulting in a high ICE of 83.3% (Figure 9c). However, pure MnP_4 electrodes exhibited a rapid capacity fade, retaining only 617 mAh g^{-1} after 40 cycles at 50 mA g^{-1}. In contrast, the MnP_4/G20 composite demonstrated enhanced cycling stability, retaining 627 mAh g^{-1} after 100 cycles at 50 mA g^{-1}, which corresponds to a capacity retention of 87.3%. Moreover, the composite exhibited outstanding rate performance, achieving a capacity of 385 mAh g^{-1} at 2000 mA g^{-1} (Figure 9d). Graphene played a critical role in addressing the challenges of P-rich materials, such as substantial volume expansion and low electrical conductivity. As shown in Figure 9e,f, through incorporating graphene, the volume expansion of the MnP_4/G20 electrode was significantly reduced from 228% to 153%, effectively minimizing mechanical stress and particle agglomeration.
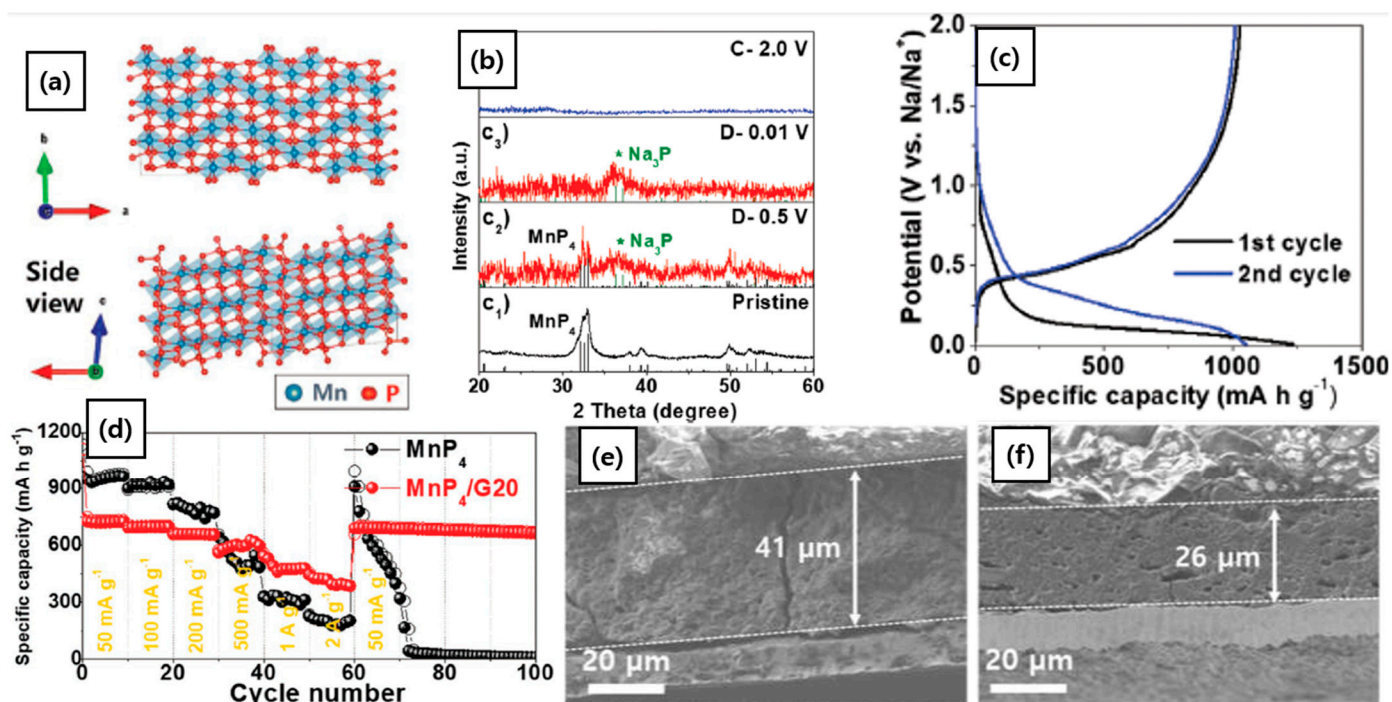
Figure 9. (**a**) Crystal structure and (**b**) ex situ XRD patterns for pristine, discharged to 0.5 V, discharged to 0.01 V, and charged to 2.0 V vs. Na/Na⁺, and (**c**) voltage profiles at a current density of 50 mA g⁻¹ of MnP₄, respectively. (**d**) Rate capabilities of MnP₄ and MnP₄/G20 electrodes. Cross sectional SEM images of fully sodiated states (0.01 V vs. Na/Na⁺) at 50 mA g⁻¹ for (**e**) MnP₄ and (**f**) MnP₄/G20 electrodes, respectively. Reproduced with permission [73]. Copyright 2021, WILEY-VCH.

3.3. Metal Antimonides as Anode Materials

Antimony (Sb) has gained considerable attention for SIBs due to their ability to accommodate three sodium ions per Sb atom through alloying reactions, forming Na₃Sb and their corresponding high theoretical capacity of 660 mAh g⁻¹. However, this process is accompanied by a significant volumetric expansion of over 390%, which leads to critical challenges in practical applications [32,57]. Specifically, the unstable surface electrolyte interphase (SEI), pulverization, and aggregation during repeated sodiation/desodiation cycles are key issues. These problems stem from the large ionic radius of Na⁺ and the resulting mechanical strain in a matrix of Sb. Consequently, the formation of Na₃Sb differentiates SIB systems from LIBs and complicates the development of efficient Sb-based anodes due to differences in reaction potentials, diffusion kinetics, and structural dynamics [82].

In MSbs, the sodiation process proceeds with the electrochemical conversion reaction and the following formation of amorphous Na_xSb phases, which subsequently crystallize into hexagonal Na₃Sb. This phase transition underscores the unique interaction between Sb and Na, which is characterized by sodium's slower diffusion kinetics and larger ionic radius. Moreover, to quantify diffusion properties, they employed potentiostatic intermittent titration (PITT) alongside DFT computational calculations. Their results indicated that Na⁺ diffuses more slowly than Li⁺, with an ion migration energy barrier of 0.21 eV for Na compared to 0.11 eV for Li [83]. As a result, the slower Na diffusion promotes prolonged amorphous phase persistence, complicating the structural stability of the material. Furthermore, mechanical strain analysis revealed that long-range strain propagation in Na₃Sb facilitates amorphization. Therefore, these findings highlight the mechanical challenges of developing high-performance Sb-based anodes for SIBs.

Specifically, the coexistence of amorphous and crystalline phases during sodiation was identified using a combination of X-ray diffraction (XRD), transmission electron microscopy (TEM), and electrochemical characterization studies. Thus, these findings illustrate the diffusion-limited nature of Na ion insertion and the structural challenges posed by long-range strain propagation, which hinders the complete crystallization of Na_3Sb into a thermodynamically stable hexagonal phase.

Finally, based on these backgrounds, which remained the still-unresolved phase formation mechanisms, Sb-based anode materials, like other metal pnictogenides (such as MNs and MPs), have been the subject of research focusing on improving Na^+ storage performance. MSbs with various chemical compositions of $FeSb_2$, $NiSb$, Cu_2Sb, Zn_4Sb_3, Mo_3Sb_7, $SnSb$, $InSb$, and $GaSb$ have been applied to SIBs, combining robust structural properties with moderate electrochemical performances [32,57].

3.3.1. Metal-Rich Antimonides (M_aSb_b, a > b)

Baggetto et al. prepared Cu_2Sb thin films using DC magnetron sputtering in an Ar atmosphere, exhibiting a tetragonal P4/nmm structure of the Cu_2Sb phase formed in small crystallite sizes (5 to 20 nm) [84]. Mössbauer spectroscopy and X-ray absorption spectroscopy (XAS) confirmed the formation of Na_3Sb in a full discharge state and an amorphous Na-Cu-Sb phase in a partial desodiation state (1 V vs. Na/Na^+). Furthermore, the Na^+ storage mechanism of Cu_2Sb is fundamentally different from that for LIBs. For LIBs, Cu_2Sb undergoes a similar conversion mechanism but transitions between Cu_2Sb and Li_3Sb phases. In contrast, for SIBs, structural reversibility was evidenced by the transition between Cu_2Sb and Na_3Sb phases during the charge/discharge process, with XRD and Mössbauer spectroscopy identifying an intermediate amorphous Na-Cu-Sb phase during the sodiation and recrystallization of Cu_2Sb upon desodiation. The formation of this intermediate phase is attributed to the gradual insertion of Na ions into the Cu_2Sb lattice, disrupting the original structure to generate an amorphous Na-Cu-Sb matrix before the full conversion to Na_3Sb. Electrochemical tests demonstrated that the use of fluoroethylene carbonate (FEC) significantly improved capacity retention, maintaining 250 mAh g^{-1} over 200 cycles at 80 µA cm^{-2}, while nanoscale film architecture and robust solid electrolyte interphase (SEI) formation contributed to the high-rate performance. Typical electrochemical potential profiles exhibit a reversible capacity of 250 mAh g^{-1} with an ICE of 61.7% during the first cycles at 20 µA cm^{-2}. In short, the key difference lies in the ionic radius and bonding characteristics of Na and Li, with sodium requiring a larger interstitial volume, leading to distinct intermediate phases in SIBs compared to the direct lithiation pathway in LIBs. Compared to pure Sb, Cu_2Sb offers enhanced stability by mitigating volume expansion through its intermetallic nature, outperforming other intermetallic compounds, like SnSb and AlSb, in terms of reversibility and Na ion transport efficiency.

Through the work of Yassar et al., Zn_4Sb_3 nanowires have emerged as a promising anode material for SIBs due to their observed rapid sodiation/desodiation kinetics [85]. Synthesized via a self-catalyzed vapor transport technique, $SbCl_3$ was vaporized at 280 °C and deposited on Zn foils maintained at 400 °C under a H_2 atmosphere, yielding single-crystal nanowires with a β-Zn_4Sb_3 phase and a rhombohedral structure (space group R3c), as confirmed via XRD and HAADF imaging. The β-phase Zn_4Sb_3 exhibits excellent electrical conductivity of 5×10^4 S m^{-1} at room temperature, which is 25 times higher than that of amorphous carbon (2×10^3 S m^{-1}). Interestingly, Zn_4Sb_3, an intermetallic compound composed of the electrochemically active metals Zn and Sb, exhibits the following energy storage mechanism. The electrochemical mechanism involves a stepwise transformation during the Na ion storage. After the first cycle (the first sodiation process: Zn_4Sb_3 + Na^+ + e^- → Na_3Sb + $NaZn_{13}$; and the first desodiation process: Na_3Sb + $NaZn_{13}$ → $NaZnSb$ + Zn

+ Na^+ + e^-), the second sodiation process can be expressed as $NaZnSb + Zn + Na^+ + e^- \rightarrow Na_3Sb + NaZn_{13}$ (Figure 10a,b). In subsequent cycles, a highly reversible pathway is established whereby NaZnSb and Zn repeatedly transition back and forth to Na_3Sb and $NaZn_{13}$ (Figure 10c). These transformations occur at an average sodiation potential of 0.58 V and a desodiation potential of 0.43 V, enabling efficient energy storage with minimal degradation. The Zn_4Sb_3 nanowires maintained a reversible capacity of 355 mAh g^{-1} at 0.1 C and 187 mAh g^{-1} at 5 C, with cycling stability showing a coulombic efficiency improvement from 45% to 99% over 50 cycles at 1 C (Figure 10d–f). This study demonstrates excellent cycling stability, rate capability, and structural robustness, paving the way for advanced intermetallic anode designs.
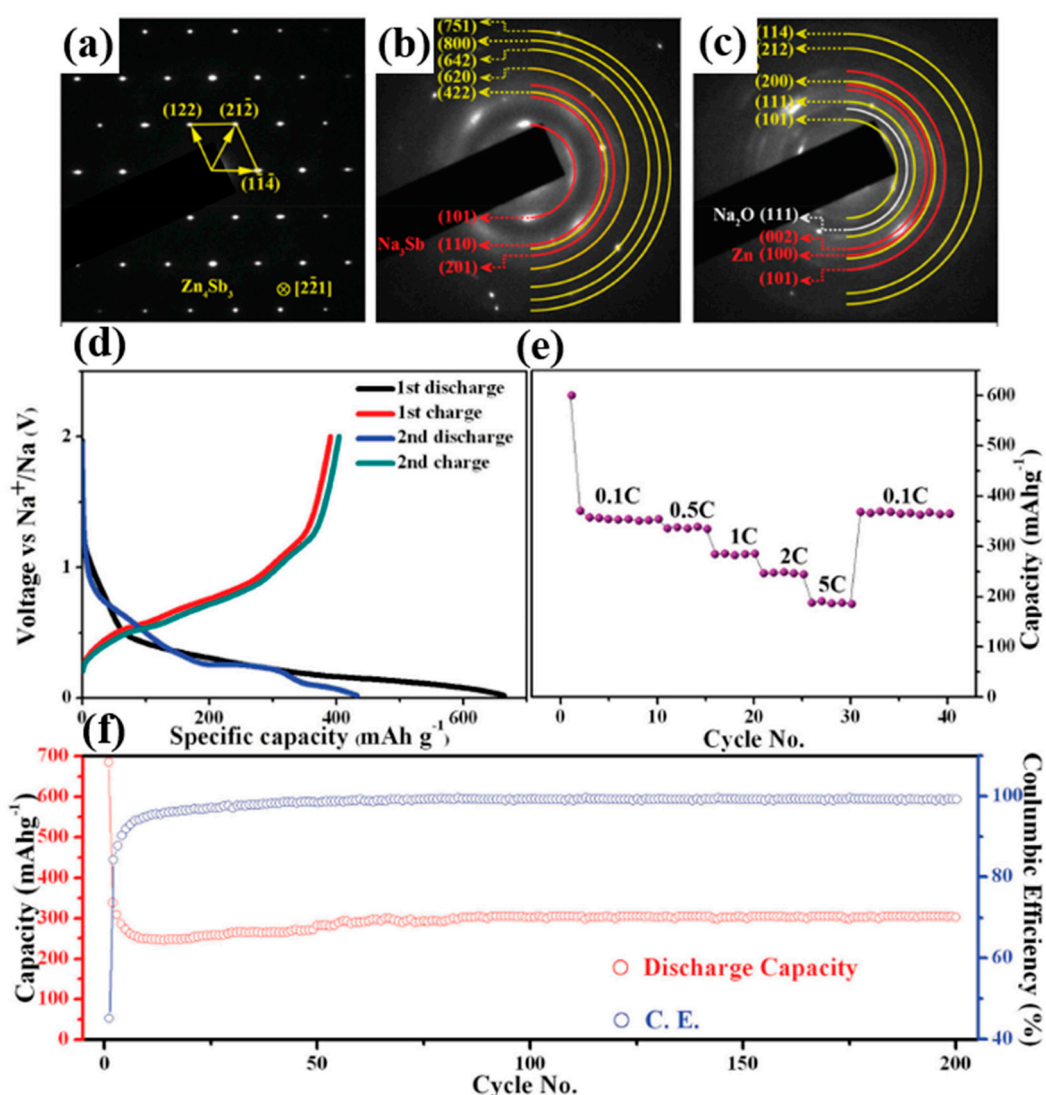
Figure 10. Electron diffraction patterns of Zn_4Sb_3 nanowires (**a**) in pristine condition, (**b**) after the first sodiation, and (**c**) after the first desodiation. (**d**) Voltage profiles at a current density of 0.5 C (1 C = 414 mA g^{-1}), (**e**) rate capabilities at different current densities, and (**f**) cycle performance at a current density of 1 C for Zn_4Sb_3 nanowires, respectively. Reproduced with permission [85]. Copyright 2016, WILEY-VCH.

3.3.2. Metal Mono-Antimonides (M_aSb_b, a = b)

SnSb exhibits a hybrid mechanism of conversion and alloying reactions, like other pnictogenides, such as Sn_4P_3 and Sn_3N_4, which contain cations with electrochemically active Sn in the compounds. Ji et al. investigated porous carbon nanofiber (CNF)-supported

SnSb nanocomposites as anode materials for SIBs to address structural degradation and enhance electrochemical performance [86]. The synthesis of these nanocomposites involved electrospinning and an additional two-step thermal process to yield interconnected porous CNF networks (40 wt.%) with uniformly dispersed SnSb nanoparticles (average size ~30 nm). Despite a low ICE of 58.5% achieved in the CNF-SnSb composite electrode, an initial reversible capacity of 392 mAh g^{-1} was delivered at 50 mA g^{-1}, with an excellent capacity retention of 99.4% over 200 cycles, and a robust rate capability, exhibiting a reversible capacity of 110 mAh g^{-1} at 1.0 A g^{-1}, was achieved. During the initial sodiation process, Sn and Sb underwent alloying reactions—each with Na ions—to form $Na_{15}Sn_4$ and Na_3Sb, respectively. In subsequent cycles, stable dealloying and alloying reactions were facilitated via the stabilization of SEI layers. In conclusion, yhe SnSb nanocomposite undergoes significant volume expansion due to sequential conversion and alloying reactions involving both Sn and Sb. However, these degradation characteristics were effectively suppressed, resulting in remarkably high cycle retention.

Ji et al. presented research on nanoporous indium-antimony (np-InSb) as a promising anode material for SIBs, aiming to address the challenge of volume expansion during cycling. The np-InSb was synthesized through a single-step chemical dealloying process using a Mg-In-Sb precursor, resulting in a porous structure [87]. This architecture, comprising both cubic- and hexagonal-structure (C/H-InSb) phases formed via the in situ alloying of In and Sb, featured interconnected ligaments with dimensions of 94 nm and 18.7 nm (Figure 11a,b). This unique design enables rapid electrolyte infiltration, accommodates volumetric changes, and facilitates electron transport. The C/H-InSb electrode delivers a high initial reversible capacity of 531.5 mAh g^{-1} at 0.2 A g^{-1}, with a relatively high ICE of 75% (Figure 11c). Over 100 cycles, it retained a capacity of 436.3 mAh g^{-1}, outperforming conventional indium-based electrodes (Figure 11d). Notably, rate capability tests demonstrate its ability to sustain a reversible capacity of 200 mAh g^{-1} at 15 A g^{-1}, showcasing its robust cycling stability. As shown in Figure 11e, operando XRD provided insights into the Na ion storage mechanism, identifying a two-step (de)alloying reaction, namely, InSb + 5 Na$^+$ + 5 e$^-$ → Na_2In + Na_3Sb, with the formation of an intermediate amorphous phase (a-Na_x(In,Sb)). This study underscores the effectiveness of porous architecture and alloying strategies in improving the stability and capacity of alloy-based anodes for SIBs.
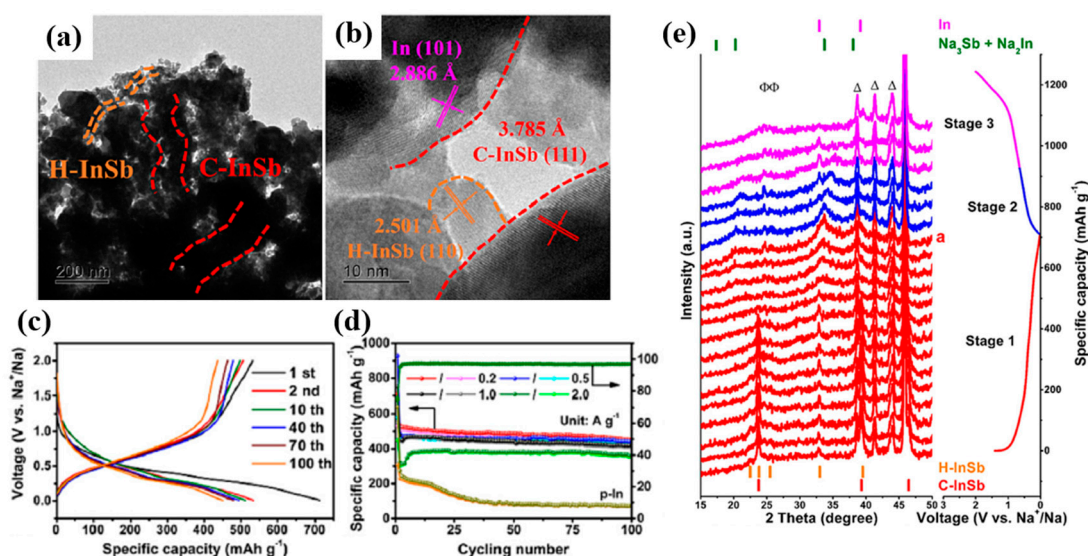
Figure 11. (**a**) TEM and (**b**) HR-TEM images; (**c**) voltage profiles at a current density of 200 mA g^{-1}; (**d**) cycling performances at different current densities; and (**e**) operando XRD results of the np-InSb during the first cycle for SIBs. Reproduced with permission [87]. Copyright 2022, Elsevier Ltd.

3.3.3. Sb-Rich Antimonides (M_aSb_b, a < b)

Edison et al. conducted a study on the Fe-Sb intermetallic alloy as a promising anode material for SIBs [88]. As shown in Figure 12a–c, the as-synthesized alloy ribbons primarily contained orthorhombic structure of $FeSb_2$ (88.38%), with a minor hexagonal structure of the FeSb phase (11.62%), as confirmed via XRD. A galvanostatic discharge/charge test indicated an initial specific capacity of 555 mAh g^{-1}, with a high ICE of 81.3%. The material retained 95% of its capacity over 80 cycles at 50 mA g^{-1} and demonstrated a robust rate capability with a reversible capacity of 300 mAh g^{-1} at 1 A g^{-1} (Figure 12d,e). Ex situ XRD and cyclic voltammetry analyses revealed a reversible sodiation mechanism, involving Na_3Sb and an amorphous Fe matrix, which provided structural stability and buffered volume changes. In full-cell configuration with a sodium manganese oxide (NMO) cathode, the Fe-Sb alloy delivered an initial capacity of 350 mAh g^{-1} (based on anode mass), a CE exceeding 99%, and retained 79% of its capacity at 50 mA g^{-1} during 50 cycles. The melt-spinning process proved effective for large-scale production, maintaining material integrity while ensuring high yields.
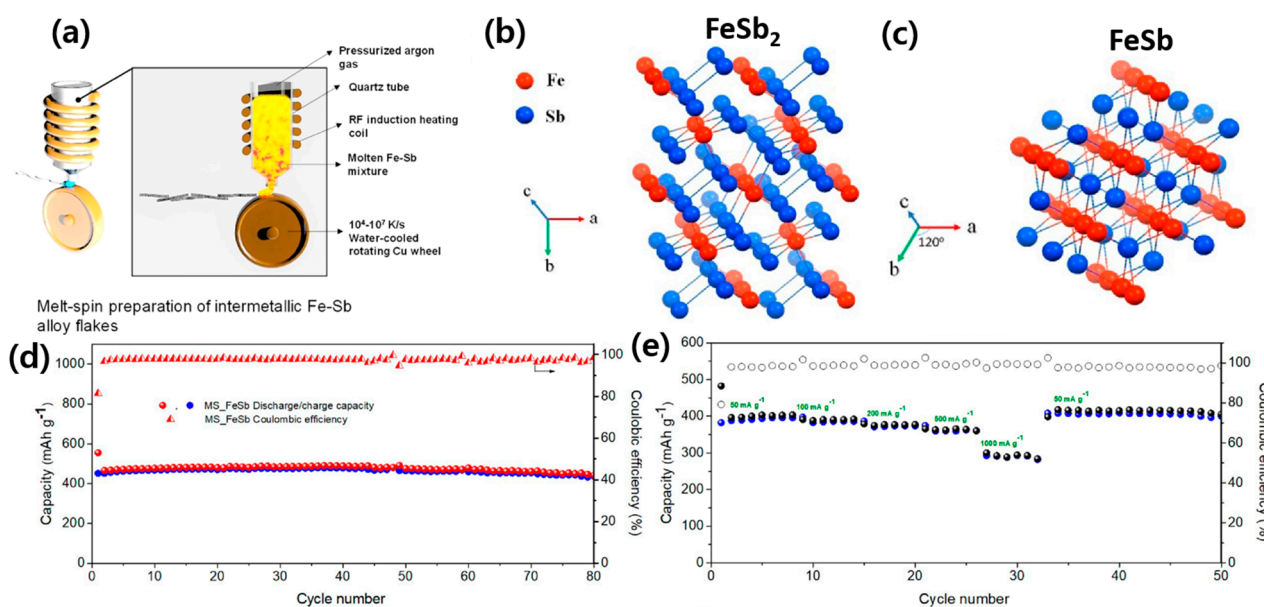
Figure 12. (**a**) Graphical illustration of the preparation of melt-spun Fe-Sb alloy ribbons and crystal structures of (**b**) $FeSb_2$ and (**c**) FeSb. (**d**) Cycle performance of Fe-Sb electrode at a current density of 50 mA g^{-1} and (**e**) rate capabilities of Fe-Sb electrode at different current densities, respectively. Reproduced with permission [88]. Copyright 2017, American Chemical Society.

Baggetto et al. investigated the potential of Mo_3Sb_7 thin films as an anode material for SIBs, emphasizing their synthesis, structural properties, and electrochemical performance [89]. The films were synthesized by heating stoichiometric Mo and Sb powders at 780 °C under a reducing atmosphere to form a Mo_3Sb_7 target, followed by deposition onto Cu substrates using magnetron sputtering. XRD and selected area electron diffraction (SAED) analyses confirmed that the films were amorphous, with a measured Sb/Mo ratio of 2.34, aligning with the theoretical composition (molar ratio of 3:7). Despite their amorphous nature, the films exhibited short-range atomic ordering the cubic structure of Mo_3Sb_7 (space group of Im$\bar{3}$m), as indicated by broad humps in the XRD pattern. Mo_3Sb_7 delivered an initial discharge and charge capacities of 470 and 330 mAh g^{-1} at 40 mA cm^{-2} with an ICE of 70%. At a high current density of 630 mA cm^{-2}, the material retained a capacity of 280 mAh g^{-1}, demonstrating excellent rate capability. Challenges included capacity fade beyond 30–40 cycles, attributed to significant volume expansion (300%) during sodiation which induced mechanical stress. For Mo_3Sb_7, the calculated expansion for the formation

of 3 Mo^0 + 7 Na_3Sb is about 300%, whereas the expansion for 3 Mo^0 + 7 Li_3Sb is 148%. This drastic difference in volume expansion contributes to more severe mechanical stress in Na ion storage, leading to reduced capacity retention and poorer cycling stability compared to their Li counterparts. To mitigate this issue, Baggetto et al. investigated the use of fluoroethylene carbonate (FEC) as an electrolyte additive to stabilize the solid electrolyte interphase (SEI). With FEC, the cycle life of Mo_3Sb_7 was significantly improved; the additive promoted the formation of an inorganic-rich SEI layer (e.g., NaF), which provided better protection for the electrode surface against side reactions.

4. Addressing Challenges in Pnictogenides to be Applied for Commercial Electrodes

SIBs have garnered attention as a sustainable and cost-effective alternative to LIBs due to the abundance of Na resources and their potential for large-scale energy storage applications. However, achieving high energy density and long-term cycling stability in SIBs remains challenging due to the larger and heavier nature of Na ion compared to Li ions. Among the multiple technological barriers, the replacement of graphite anode, which is less active with Na ions, with hard carbon (HC) has emerged as a critical issue for the commercialization of SIBs. HC, a non-graphitizable carbon material, possesses moderate capacity (~300 mAh g^{-1} at a low current density) and low working potential (0.1 V vs. Na/Na^+), with lower prices [90]. The electrochemical performance of the HC electrode can further be improved by integrating with pnictogenide compounds, which showed higher reversible capacity and lower working potential as anodes for SIBs compared to those of other anode materials such as oxide or sulfide materials (Figure 13 and Table 2).

In particular, more explorations into high-capacity anode candidates as pnictogen-rich compounds (e.g., P-rich MPs, N-rich MNs, or Sb-rich MSbs), along with their mass productive synthesis processes, are urgently required in order to achieve commercially available HC–pnictogenide composites. Pnictogen-rich compounds with higher reversible capacities can reduce the added amounts of pnictogenides needed to achieve the target capacity for composite electrode and thus contribute to lowering the prices of composite fabrication. While the synthesis process of pnictogenides has been widely developed, including the high-energy mechanical milling (HEMM) process, chemical vapor deposition (CVD), and the solvothermal process [46,57,91], further advancements in the facile synthesis process and its process parameters for mass-production are essential in order to properly consider the commercialization of pnictogenides. Along with the development of a mass productive synthetic process for pnictogenides, the reactions and processes used for their recycling will play an increasingly important role from an environmental perspective, improving the sustainability of pnictogenides as anodes for SIBs [92].

To effectively combine hard carbon and high capacity pnictogenides, multi-dimensional carbonaceous materials, like 1D of CNTs or 2D of graphenes, should be considered and designed to form 3D electrically conductive networks for composite materials. This strategy can suppress the large volume expansion of pnictogenides, enhance electrical and ionic conductivities, and optimize electrochemical performance, paving the way for the commercialization of SIBs. For instance, P-rich MPs composites (e.g., MnP_4/G20 or NiP_3@CNT) and N-rich MNs composites (e.g., MnN/rGO) offer a highly reversible capacity and improved cycling performance when combined with advanced carbon coatings such as CNTs, graphene, or reduced graphene oxide (rGO).

In the fabrication of composite electrodes for next-generation SIBs, a similar strategy would be applied to that of commercialized LIBs, combining the conventional graphite anode and small amounts (5–10 wt.%) of high-capacity silicon anode to balance the high energy density and cycle stability at the same time [93]. This guideline can be applied to the design of HC/metal pnictogenide composites for SIBs by incorporating small

quantities of pnictogenides into HC matrices, enabling gradual improvements in energy density and cycling performance [94–96].

Optimizing electrolyte systems is one of the critical factors for enhancing SIB performance. Previous studies have shown that optimized electrolytes like 1 M NaPF$_6$ in diglyme minimize side reactions and enhance SEI stability. Mogensen et al. demonstrated that unconventional electrolytes, including glymes and carbonates, improve SIB performance by stabilizing the SEI layer on high-capacity electrodes [97]. Chang et al. identified EC/PC blends as suitable for HC electrodes due to their ability to form stable SEI layers [98]. Additives like fluoroethylene carbonate (FEC) and vinylene carbonate (VC) also enhance SEI stability, improving the cycling performance of anode materials with large volume changes [99]. Toward developing commercial electrolyte systems for SIBs, extensive research is critically needed to design electrolyte systems capable of simultaneously forming stable SEI layers on both surfaces of HC matrices and pnictogenides.

Applying an advanced binder system is also a feasible approach to addressing the challenges faced by pnictogenides with high theoretical capacities. In LIBs, several strategies have been widely performed, such as cross-linking, self-healing, and conductivity-enhancing binders, addressing volume expansion and structural degradation in high-capacity electrodes [100,101]. While these innovations have not yet been systematically applied in SIB systems, further research should aim to modify and integrate strategies for commercial binder systems, including polyvinylidene fluoride (PVDF), carboxymethyl cellulose (CMC), and polyacrylic acid (PAA), to enhance their suitability for commercialization in SIBs [102].

In conclusion, the integration of HC with pnictogen-rich pnictogenides, combined with advanced coating or mixing strategies with CNTs, graphene, or rGO, along with the optimization of binder and electrolyte systems, address the above challenges. The synergistic design of such composites can provide a pathway to achieving high energy density, robust cycling stability, and scalability for sustainable energy storage systems.
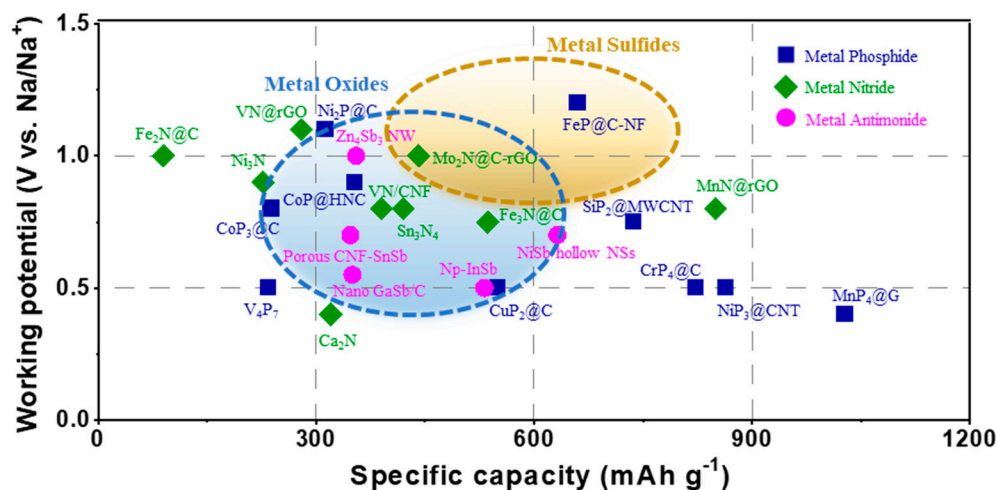
Figure 13. Comparisons of working potential and specific capacity, corresponding to metal pnictogenides, oxides, and sulfides in the Na-ion battery system.

Table 2. State-of-the-art performance of metal pnictogenides, including nitrides, phosphides, and antimonites, as anode materials for SIBs.

System	Materials	Working Potential (V vs. Na/Na$^+$)	Specific Capacity (mAh g^{-1})	Current Density (mA g^{-1})	I.C.E. (%)	Ref.
Metal nitrides (MNs)	Ni$_3$N	0.9	227	42	50	[60]
	Fe$_3$N@C/3DNCF	0.75	536	200	56.4	[62]
	Fe$_2$N@C	1.0	93	500	60	[103]
	Ca$_2$N	0.4	320	50	30	[61]
	Mo$_2$N@C-rGO	1.0	441	200	42.3	[63]
	VN@rGO	1.1	280	50	12	[65]
	VN/CNF	0.8	390	100	49.2	[64]
	MnN@rGO	0.8	850	250	52.14	[66]
	Sn$_3$N$_4$	0.8	420	200	32	[68]
Metal phosphides (MPs)	Ni$_2$P@C	1.1	313	100	67	[77]
	CoP/HNC	0.9	353	100	50.35	[79]
	FeP@C-NF	1.2	660	100	69.8	[78]
	V$_4$P$_7$	0.5	234	100	69.97	[70]
	CuP$_2$@C	0.5	550	50	67.14	[81]
	SiP$_2$@MWCNT	0.75	737	100	73.04	[104]
	CoP$_3$@C	0.8	238	100	79	[105]
	NiP$_3$@CNT	0.5	864	100	64.6	[72]
	CrP$_4$@C	0.5	823	50	76.3	[74]
	MnP$_4$@G	0.4	1028	50	83.3	[73]
Metal antimonides (MSbs)	CNF-SnSb	0.6	347	100	53	[86]
	np-InSb	0.5	531.5	200	74.7	[87]
	nano GaSb/C	0.6	350	50	76.8	[106]
	NiSb NSs	0.7	632	60	37.6	[107]
	Zn$_4$Sb$_3$ NW	0.25	355	41.4	45	[85]

5. Conclusions

In this review, we outline and summarize the electrochemical performance of pnictogenides as potential candidates in next-generation, high-capacity anode materials for sodium-ion batteries (SIBs). Their unique physical and chemical properties affect the Na-ion's storage mechanism and properties across various compositions and crystal structures. Specifically, pnictogen-rich compositions in M$_a$X$_b$ compound systems (X = N, P, or Sb) are identified as promising candidates due to their high theoretical capacities and appropriate operating voltages, which address key challenges in SIBs. However, these pnictogen-rich compounds face significant obstacles, such as structural instability caused by large volume changes, low electronic conductivities, and poor initial coulombic efficiencies. To overcome these limitations, strategies such as forming composites with conductive carbon-based materials have been proposed. Moreover, incorporating small amounts of pnictogen-rich metal pnictogenides coated with highly conductive carbon-based materials (e.g., CNTs, graphene, or rGO) into a hard carbon matrix as a composite electrode has been highlighted as a critical approach for achieving successful SIB commercialization. The optimization process of the SEI layers formed on both surfaces of the composite materials is also a critical point to be addressed with further studies. Additionally, addressing challenges in terms of both the mass productive synthesis process and the sustainable recycling method for pnictogenides will be essential to position SIBs as competitive and eco-friendly alternatives to LIBs in energy storage markets. With experimental

validation and engineering innovations performed, pnictogenides demonstrate significant potential, implementing sustainable and high-performance SIBs, paving the way for their widespread adoption.

References

1. Hasan, M.K.; Mahmud, M.; Ahasan Habib, A.K.M.; Motakabber, S.M.A.; Islam, S. Review of electric vehicle energy storage and management system: Standards, issues, and challenges. *J. Energy Storage* **2021**, *41*, 102940. https://doi.org/10.1016/j.est.2021.102940.

2. Butt, F.S.; Lewis, A.; Chen, T.; Mazlan, N.A.; Wei, X.; Hayer, J.; Chen, S.; Han, J.; Yang, Y.; Yang, S.; et al. Lithium Harvesting from the Most Abundant Primary and Secondary Sources: A Comparative Study on Conventional and Membrane Technologies. *Membranes* **2022**, *12*, 373. https://doi.org/10.3390/membranes12040373.

3. Tian, Y.; Zeng, G.; Rutt, A.; Shi, T.; Kim, H.; Wang, J.; Koettgen, J.; Sun, Y.; Ouyang, B.; Chen, T.; et al. Promises and Challenges of Next-Generation "Beyond Li-ion" Batteries for Electric Vehicles and Grid Decarbonization. *Chem. Rev.* **2021**, *121*, 1623–1669. https://doi.org/10.1021/acs.chemrev.0c00767.

4. Liang, Y.; Dong, H.; Aurbach, D.; Yao, Y. Current status and future directions of multivalent metal-ion batteries. *Nat. Energy* **2020**, *5*, 646–656. https://doi.org/10.1038/s41560-020-0655-0.

5. Rostami, H.; Valio, J.; Suominen, P.; Tynjälä, P.; Lassi, U. Advancements in cathode technology, recycling strategies, and market dynamics: A comprehensive review of sodium ion batteries. *Chem. Eng. J.* **2024**, *495*, 153471. https://doi.org/10.1016/j.cej.2024.153471.

6. Mohan, I.; Raj, A.; Shubham, K.; Lata, D.B.; Mandal, S.; Kumar, S. Potential of potassium and sodium-ion batteries as the future of energy storage: Recent progress in anodic materials. *J. Energy Storage* **2022**, *55*, 105625. https://doi.org/10.1016/j.est.2022.105625.

7. Wu, J.; Ihsan-Ul-Haq, M.; Ciucci, F.; Huang, B.; Kim, J.-K. Rationally designed nanostructured metal chalcogenides for advanced sodium-ion batteries. *Energy Storage Mater.* **2021**, *34*, 582–628. https://doi.org/10.1016/j.ensm.2020.10.007.

8. Ghahari, A.; Raissi, H. Architectural design of anode materials for superior alkali-ion (Li/Na/K) batteries storage. *Sci. Rep.* **2024**, *14*, 3959. https://doi.org/10.1038/s41598-024-54214-6.

9. Li, Y.; Lu, Y.; Adelhelm, P.; Titirici, M.-M.; Hu, Y.-S. Intercalation chemistry of graphite: Alkali metal ions and beyond. *Chem. Soc. Rev.* **2019**, *48*, 4655–4687. https://doi.org/10.1039/C9CS00162J.

10. Yang, Y.; Wu, C.; He, X.-X.; Zhao, J.; Yang, Z.; Li, L.; Wu, X.; Li, L.; Chou, S.-L. Boosting the Development of Hard Carbon for Sodium-Ion Batteries: Strategies to Optimize the Initial Coulombic Efficiency. *Adv. Funct. Mater.* **2024**, *34*, 2302277. https://doi.org/10.1002/adfm.202302277.

11. Chu, Y.; Zhang, J.; Zhang, Y.; Li, Q.; Jia, Y.; Dong, X.; Xiao, J.; Tao, Y.; Yang, Q.-H. Reconfiguring Hard Carbons with Emerging Sodium-Ion Batteries: A Perspective. *Adv. Mater.* **2023**, *35*, 2212186. https://doi.org/10.1002/adma.202212186.

12. Zhang, C.; Wang, F.; Han, J.; Bai, S.; Tan, J.; Liu, J.; Li, F. Challenges and Recent Progress on Silicon-Based Anode Materials for Next-Generation Lithium-Ion Batteries. *Small Struct.* **2021**, *2*, 2100009. https://doi.org/10.1002/sstr.202100009.

13. Loaiza, L.C.; Monconduit, L.; Seznec, V. Si and Ge-Based Anode Materials for Li-, Na-, and K-Ion Batteries: A Perspective from Structure to Electrochemical Mechanism. *Small* **2020**, *16*, 1905260. https://doi.org/10.1002/smll.201905260.

14. Zhang, J.; Zheng, T.; Cheng, K.-w.E.; Lam, K.-h.; Boles, S.T. Insights into the Sodiation Kinetics of Si and Ge Anodes for Sodium-Ion Batteries. *J. Electrochem. Soc.* **2023**, *170*, 100518. https://doi.org/10.1149/1945-7111/ad0075.

15. Li, L.; Zheng, Y.; Zhang, S.; Yang, J.; Shao, Z.; Guo, Z. Recent progress on sodium ion batteries: Potential high-performance anodes. *Energy Environ. Sci.* **2018**, *11*, 2310–2340. https://doi.org/10.1039/C8EE01023D.

16. Ali, Z.; Zhang, T.; Asif, M.; Zhao, L.; Yu, Y.; Hou, Y. Transition metal chalcogenide anodes for sodium storage. *Mater. Today* **2020**, *35*, 131–167. https://doi.org/10.1016/j.mattod.2019.11.008.

17. Wu, C.; Dou, S.-X.; Yu, Y. The State and Challenges of Anode Materials Based on Conversion Reactions for Sodium Storage. *Small* **2018**, *14*, 1703671. https://doi.org/10.1002/smll.201703671.

18. Kumar Prajapati, A.; Bhatnagar, A. A review on anode materials for lithium/sodium-ion batteries. *J. Energy Chem.* **2023**, *83*, 509–540. https://doi.org/10.1016/j.jechem.2023.04.043.

19. Zhang, H.; Hasa, I.; Passerini, S. Beyond Insertion for Na-Ion Batteries: Nanostructured Alloying and Conversion Anode Materials. *Adv. Energy Mater.* **2018**, *8*, 1702582. https://doi.org/10.1002/aenm.201702582.

20. Chen, F.; Xu, J.; Wang, S.; Lv, Y.; Li, Y.; Chen, X.; Xia, A.; Li, Y.; Wu, J.; Ma, L. Phosphorus/Phosphide-Based Materials for Alkali Metal-Ion Batteries. *Adv. Sci.* **2022**, *9*, 2200740. https://doi.org/10.1002/advs.202200740.

21. Zhang, Y.; Zhou, Q.; Zhu, J.; Yan, Q.; Dou, S.X.; Sun, W. Nanostructured Metal Chalcogenides for Energy Storage and Electrocatalysis. *Adv. Funct. Mater.* **2017**, *27*, 1702317. https://doi.org/10.1002/adfm.201702317.

22. Wu, X.; Lan, X.; Hu, R.; Yao, Y.; Yu, Y.; Zhu, M. Tin-Based Anode Materials for Stable Sodium Storage: Progress and Perspective. *Adv. Mater.* **2022**, *34*, 2106895. https://doi.org/10.1002/adma.202106895.

23. Wang, H.; Li, J.; Li, K.; Lin, Y.; Chen, J.; Gao, L.; Nicolosi, V.; Xiao, X.; Lee, J.-M. Transition metal nitrides for electrochemical energy applications. *Chem. Soc. Rev.* **2021**, *50*, 1354–1390. https://doi.org/10.1039/D0CS00415D.

24. Gao, B.; Li, X.; Ding, K.; Huang, C.; Li, Q.; Chu, P.K.; Huo, K. Recent progress in nanostructured transition metal nitrides for advanced electrochemical energy storage. *J. Mater. Chem. A* **2019**, *7*, 14–37. https://doi.org/10.1039/C8TA05760E.

25. Zhang, W.; Liu, T.; Wang, Y.; Liu, Y.; Nai, J.; Zhang, L.; Sheng, O.; Tao, X. Strategies to improve the performance of phosphide anodes in sodium-ion batteries. *Nano Energy* **2021**, *90*, 106475. https://doi.org/10.1016/j.nanoen.2021.106475.

26. Li, Z.; Zheng, Y.; Liu, Q.; Wang, Y.; Wang, D.; Li, Z.; Zheng, P.; Liu, Z. Recent advances in nanostructured metal phosphides as promising anode materials for rechargeable batteries. *J. Mater. Chem. A* **2020**, *8*, 19113–19132. https://doi.org/10.1039/D0TA06533A.

27. Patel, P.C.; Awasthi, S.; Mishra, P.K.; Lakharwal, P.; Kashyap, J. Fe–As Intermetallic Alloys: A Way Out for Sodium-Ion Batteries. *Energy Fuels* **2023**, *37*, 16062–16071. https://doi.org/10.1021/acs.energyfuels.3c02138.

28. Chen, W.; Yang, J.; Chen, J.; Bruch, J. Exposures to silica mixed dust and cohort mortality study in tin mines: Exposure-response analysis and risk assessment of lung cancer. *Am. J. Ind. Med.* **2006**, *49*, 67–76. https://doi.org/10.1002/ajim.20248.

29. Jomova, K.; Jenisova, Z.; Feszterova, M.; Baros, S.; Liska, J.; Hudecova, D.; Rhodes, C.J.; Valko, M. Arsenic: Toxicity, oxidative stress and human disease. *J. Appl. Toxicol.* **2011**, *31*, 95–107. https://doi.org/10.1002/jat.1649.

30. Tanaka, A. Toxicity of indium arsenide, gallium arsenide, and aluminium gallium arsenide. *Toxicol. Appl. Pharmacol.* **2004**, *198*, 405–411. https://doi.org/10.1016/j.taap.2003.10.019.

31. Sarkar, S.; Peter, S.C. An overview on Sb-based intermetallics and alloys for sodium-ion batteries: Trends, challenges and future prospects from material synthesis to battery performance. *J. Mater. Chem. A* **2021**, *9*, 5164–5196. https://doi.org/10.1039/D0TA12063D.

32. Chen, B.; Liang, M.; Wu, Q.; Zhu, S.; Zhao, N.; He, C. Recent Developments of Antimony-Based Anodes for Sodium- and Potassium-Ion Batteries. *Trans. Tianjin Univ.* **2022**, *28*, 6–32. https://doi.org/10.1007/s12209-021-00304-9.

33. Hao, Y.; Shao, J.; Yuan, Y.; Li, X.; Xiao, W.; Sari, H.M.K.; Liu, T.; Lu, J. Design of Phosphide Anodes Harvesting Superior Sodium Storage: Progress, Challenges, and Perspectives. *Adv. Funct. Mater.* **2023**, *33*, 2212692. https://doi.org/10.1002/adfm.202212692.

34. Dong, S.; Chen, X.; Zhang, X.; Cui, G. Nanostructured transition metal nitrides for energy storage and fuel cells. *Coord. Chem. Rev.* **2013**, *257*, 1946–1956. https://doi.org/10.1016/j.ccr.2012.12.012.

35. Zhong, Y.; Xia, X.H.; Shi, F.; Zhan, J.Y.; Tu, J.P.; Fan, H.J. Transition metal carbides and nitrides in energy storage and conversion. *Adv. Sci.* **2015**, *3*, 1500286. https://doi.org/10.1002/advs.201500286.

36. Lengauer, W. Diffusional control of the near-surface microstructure in functional gradient hardmetals. *Mater. Und Werkst.* **2005**, *36*, 460–466. https://doi.org/10.1002/mawe.200500906.

37. Idrees, M.; Mukhtar, A.; Ata ur, R.; Abbas, S.M.; Zhang, Q.; Li, X. Transition metal nitride electrodes as future energy storage devices: A review. *Mater. Today Commun.* **2021**, *27*, 102363. https://doi.org/10.1016/j.mtcomm.2021.102363.

38. Chen, K.; Pathak, R.; Gurung, A.; Adhamash, E.A.; Bahrami, B.; He, Q.; Qiao, H.; Smirnova, A.L.; Wu, J.J.; Qiao, Q.; et al. Flower-shaped lithium nitride as a protective layer via facile plasma activation for stable lithium metal anodes. *Energy Storage Mater.* **2019**, *18*, 389–396. https://doi.org/10.1016/j.ensm.2019.02.006.

39. Wang, X.; Chen, Z.; Xue, X.; Wang, J.; Wang, Y.; Bresser, D.; Liu, X.; Chen, M.; Passerini, S. Achieving stable lithium metal anode via constructing lithiophilicity gradient and regulating Li$_3$N-rich SEI. *Nano Energy* **2025**, *133*, 110439. https://doi.org/10.1016/j.nanoen.2024.110439.

40. Balogun, M.-S.; Huang, Y.; Qiu, W.; Yang, H.; Ji, H.; Tong, Y. Updates on the development of nanostructured transition metal nitrides for electrochemical energy storage and water splitting. *Mater. Today* **2017**, *20*, 425–451. https://doi.org/10.1016/j.mattod.2017.03.019.

41. Reddy, M.V.; Prithvi, G.; Loh, K.P.; Chowdari, B.V.R. Li Storage and Impedance Spectroscopy Studies on Co$_3$O$_4$, CoO, and CoN for Li-Ion Batteries. *ACS Appl. Mater. Interfaces* **2014**, *6*, 680–690. https://doi.org/10.1021/am4047552.

42. Xu, K.; Chen, P.; Li, X.; Tong, Y.; Ding, H.; Wu, X.; Chu, W.; Peng, Z.; Wu, C.; Xie, Y. Metallic Nickel Nitride Nanosheets Realizing Enhanced Electrochemical Water Oxidation. *J. Am. Chem. Soc.* **2015**, *137*, 4119–4125. https://doi.org/10.1021/ja5119495.

43. Agarwal, A.; Sankapal, B.R. Metal phosphides: Topical advances in the design of supercapacitors. *J. Mater. Chem. A* **2021**, *9*, 20241–20276. https://doi.org/10.1039/D1TA04104E.

44. Tahri, W.; Zhou, X.; Khan, R.; Sajid, M. Recent Trends in Transition Metal Phosphide (TMP)-Based Seawater Electrolysis for Hydrogen Evolution. *Sustainability* **2023**, *15*, 14389. https://doi.org/10.3390/su151914389.

45. Lee, J.; Kim, K.-H.; Kim, H.-H.; Hong, S.-H. NiP$_2$/C nanocomposite as a high performance anode for sodium ion batteries. *Electrochim. Acta* **2022**, *403*, 139686. https://doi.org/10.1016/j.electacta.2021.139686.

46. Chang, G.; Zhao, Y.; Dong, L.; Wilkinson, D.P.; Zhang, L.; Shao, Q.; Yan, W.; Sun, X.; Zhang, J. A review of phosphorus and phosphides as anode materials for advanced sodium-ion batteries. *J. Mater. Chem. A* **2020**, *8*, 4996–5048. https://doi.org/10.1039/C9TA12169B.

47. Li, Q.; Yang, D.; Chen, H.; Lv, X.; Jiang, Y.; Feng, Y.; Rui, X.; Yu, Y. Advances in metal phosphides for sodium-ion batteries. *SusMat* **2021**, *1*, 359–392. https://doi.org/10.1002/sus2.19.

48. Liu, Y.; McCue, A.J.; Li, D. Metal Phosphides and Sulfides in Heterogeneous Catalysis: Electronic and Geometric Effects. *ACS Catal.* **2021**, *11*, 9102–9127. https://doi.org/10.1021/acscatal.1c01718.

49. Pöhls, J.-H.; Faghaninia, A.; Petretto, G.; Aydemir, U.; Ricci, F.; Li, G.; Wood, M.; Ohno, S.; Hautier, G.; Snyder, G.J.; et al. Metal phosphides as potential thermoelectric materials. *J. Mater. Chem. C* **2017**, *5*, 12441–12456. https://doi.org/10.1039/C7TC03948D.

50. Bhunia, K.; Chandra, M.; Kumar Sharma, S.; Pradhan, D.; Kim, S.-J. A critical review on transition metal phosphide based catalyst for electrochemical hydrogen evolution reaction: Gibbs free energy, composition, stability, and true identity of active site. *Coord. Chem. Rev.* **2023**, *478*, 214956. https://doi.org/10.1016/j.ccr.2022.214956.

51. Liu, W.; Zhi, H.; Yu, X. Recent progress in phosphorus based anode materials for lithium/sodium ion batteries. *Energy Storage Mater.* **2019**, *16*, 290–322. https://doi.org/10.1016/j.ensm.2018.05.020.

52. Gong, N.; Deng, C.; Wu, L.; Wan, B.; Wang, Z.; Li, Z.; Gou, H.; Gao, F. Structural Diversity and Electronic Properties of 3d Transition Metal Tetraphosphides, TMP$_4$ (TM = V, Cr, Mn, and Fe). *Inorg. Chem.* **2018**, *57*, 9385–9392. https://doi.org/10.1021/acs.inorgchem.8b01380.

53. Dwivedi, A.; Pandey, A.; Bajpai, A. Stability and electronic properties of transition metal antimonides in ionic and neutral case-TM$_m$Sb$_n$ (m, n=1-2). *J. Comput. Methods Mol. Des.* **2014**, *4*, 38–45.

54. Jing, W.T.; Yang, C.C.; Jiang, Q. Recent progress on metallic Sn- and Sb-based anodes for sodium-ion batteries. *J. Mater. Chem. A* **2020**, *8*, 2913–2933. https://doi.org/10.1039/C9TA11782B.

55. Bennett, B.; Magno, R.; Boos, J.; Kruppa, W.; Ancona, M. Antimonide-based compound semiconductors for electronic devices: A review. *Solid-State Electron.* **2005**, *49*, 1875–1895. https://doi.org/10.1016/j.sse.2005.09.008.

56. Usui, H.; Domi, Y.; Takada, N.; Sakaguchi, H. Reaction Mechanism of Indium Antimonide as a Sodium Storage Material. *Cryst. Growth Des.* **2021**, *21*, 218–226. https://doi.org/10.1021/acs.cgd.0c01045.

57. He, J.; Wei, Y.; Zhai, T.; Li, H. Antimony-based materials as promising anodes for rechargeable lithium-ion and sodium-ion batteries. *Mater. Chem. Front.* **2018**, *2*, 437–455. https://doi.org/10.1039/C7QM00480J.

58. Luo, Q.; Lu, C.; Liu, L.; Zhu, M. A review on the synthesis of transition metal nitride nanostructures and their energy related applications. *Green Energy Environ.* **2023**, *8*, 406–437. https://doi.org/10.1016/j.gee.2022.07.002.

59. Wriedt, H.A. The N-Ni (Nitrogen-Nickel) system. *Bull. Alloy Phase Diagr.* **1985**, *6*, 558–563. https://doi.org/10.1007/BF02887159.

60. Li, X.; Hasan, M.M.; Hector, A.L.; Owen, J.R. Performance of nanocrystalline Ni$_3$N as a negative electrode for sodium-ion batteries. *J. Mater. Chem. A* **2013**, *1*, 6441–6445. https://doi.org/10.1039/C3TA00184A.

61. Chen, G.; Bai, Y.; Li, H.; Li, Y.; Wang, Z.; Ni, Q.; Liu, L.; Wu, F.; Yao, Y.; Wu, C. Multilayered Electride Ca$_2$N Electrode via Compression Molding Fabrication for Sodium Ion Batteries. *ACS Appl. Mater. Interfaces* **2017**, *9*, 6666–6669. https://doi.org/10.1021/acsami.6b16186.

62. Ma, X.; Xiong, X.; Zeng, J.; Zou, P.; Lin, Z.; Liu, M. Melamine-assisted synthesis of Fe₃N featuring highly reversible crystalline-phase transformation for ultrastable sodium ion storage. *J. Mater. Chem. A* **2020**, *8*, 6768–6775. https://doi.org/10.1039/D0TA01888K.

63. Vadahanambi, S.; Park, H. Carbon sheathed molybdenum nitride nanoparticles anchored on reduced graphene oxide as high-capacity sodium-ion battery anodes and supercapacitors. *New J. Chem.* **2018**, *42*, 5668–5673. https://doi.org/10.1039/C7NJ04764A.

64. Xu, L.; Xiong, P.; Zeng, L.; Liu, R.; Liu, J.; Luo, F.; Li, X.; Chen, Q.; Wei, M.; Qian, Q. Facile fabrication of a vanadium nitride/carbon fiber composite for half/full sodium-ion and potassium-ion batteries with long-term cycling performance. *Nanoscale* **2020**, *12*, 10693–10702. https://doi.org/10.1039/C9NR10211F.

65. Wei, S.; Wang, C.; Chen, S.; Zhang, P.; Zhu, K.; Wu, C.; Song, P.; Wen, W.; Song, L. Dial the Mechanism Switch of VN from Conversion to Intercalation toward Long Cycling Sodium-Ion Battery. *Adv. Energy Mater.* **2020**, *10*, 1903712. https://doi.org/10.1002/aenm.201903712.

66. Sridhar, V.; Park, H. Manganese nitride stabilized on reduced graphene oxide substrate for high performance sodium ion batteries, super-capacitors and EMI shielding. *J. Alloys Compd.* **2019**, *808*, 151748. https://doi.org/10.1016/j.jallcom.2019.151748.

67. Li, Z.; Ding, J.; Mitlin, D. Tin and Tin Compounds for Sodium Ion Battery Anodes: Phase Transformations and Performance. *Acc. Chem. Res.* **2015**, *48*, 1657–1665. https://doi.org/10.1021/acs.accounts.5b00114.

68. Fitch, S.D.S.; Cibin, G.; Hepplestone, S.P.; Garcia-Araez, N.; Hector, A.L. Solvothermal synthesis of Sn₃N₄ as a high capacity sodium-ion anode: Theoretical and experimental study of its storage mechanism. *J. Mater. Chem. A* **2020**, *8*, 16437–16450. https://doi.org/10.1039/D0TA04034G.

69. Li, Z.; Fang, Y.; Zhang, J.; Lou, X.W. Necklace-Like Structures Composed of Fe₃N@C Yolk–Shell Particles as an Advanced Anode for Sodium-Ion Batteries. *Adv. Mater.* **2018**, *30*, 1800525. https://doi.org/10.1002/adma.201800525.

70. Kim, K.-H.; Choi, J.; Hong, S.-H. Superior electrochemical sodium storage of V₄P₇ nanoparticles as an anode for rechargeable sodium-ion batteries. *Chem. Commun.* **2019**, *55*, 3207–3210. https://doi.org/10.1039/C8CC09184F.

71. He, L.; Guo, J.; Liu, S.; Wang, F.; Li, X.; Su, Z. Progress of metal phosphides as the anode materials for sodium ion batteries. *J. Alloys Compd.* **2024**, *997*, 174924. https://doi.org/10.1016/j.jallcom.2024.174924.

72. Ihsan-Ul-Haq, M.; Huang, H.; Cui, J.; Yao, S.; Wu, J.; Chong, W.G.; Huang, B.; Kim, J.-K. Chemical interactions between red P and functional groups in NiP₃/CNT composite anodes for enhanced sodium storage. *J. Mater. Chem. A* **2018**, *6*, 20184–20194. https://doi.org/10.1039/C8TA06841K.

73. Kim, K.-H.; Hong, S.-H. Manganese Tetraphosphide (MnP₄) as a High Capacity Anode for Lithium-Ion and Sodium-Ion Batteries. *Adv. Energy Mater.* **2021**, *11*, 2003609. https://doi.org/10.1002/aenm.202003609.

74. Lee, J.; Lee, D.; Kim, K.-H.; Hong, S.-H. Chromium tetraphosphide (CrP₄) as a high-performance anode for Li ion and Na ion batteries. *J. Mater. Chem. A* **2024**, *12*, 11463–11472. https://doi.org/10.1039/D4TA00854E.

75. Zhang, J.-L.; Li, C.-L.; Wang, W.-H.; Yu, D.Y.W. Facile synthesis of hollow Cu₃P for sodium-ion batteries anode. *Rare Met.* **2021**, *40*, 3460–3465. https://doi.org/10.1007/s12598-021-01718-z.

76. Hino, M.; Iikubo, S.; Ohtani, H. Thermodynamic Analysis of the Cu-Sn-P Ternary System. *High Temp. Mater. Process.* **2011**, *30*, 387–404, doi:doi:10.1515/htmp.2011.061.

77. Zheng, J.; Huang, X.; Pan, X.; Teng, C.; Wang, N. Yolk-shelled Ni₂P@carbon nanocomposite as high-performance anode material for lithium and sodium ion batteries. *Appl. Surf. Sci.* **2019**, *473*, 699–705. https://doi.org/10.1016/j.apsusc.2018.12.225.

78. Yang, Y.; Fu, W.; Lee, D.C.; Bell, C.; Drexler, M.; Ma, Z.F.; Magasinski, A.; Yushin, G.; Alamgir, F.M. Porous FeP/C composite nanofibers as high-performance anodes for Li-ion/Na-ion batteries. *Mater. Today Energy* **2020**, *16*, 100410. https://doi.org/10.1016/j.mtener.2020.100410.

79. Huang, W.; Shangguan, H.; Zheng, X.; Engelbrekt, C.; Yang, Y.; Li, S.; Mølhave, K.; Xiao, X.; Lin, X.; Ci, L.; et al. Three-dimensional hollow nitrogen-doped carbon shells enclosed monodisperse CoP nanoparticles for long cycle-life sodium storage. *Electrochim. Acta* **2021**, *395*, 139112. https://doi.org/10.1016/j.electacta.2021.139112.

80. Wang, L.; Li, Q.; Chen, Z.; Wang, Y.; Li, Y.; Chai, J.; Han, N.; Tang, B.; Rui, Y.; Jiang, L. Metal Phosphide Anodes in Sodium-Ion Batteries: Latest Applications and Progress. *Small* **2024**, *20*, 2310426. https://doi.org/10.1002/smll.202310426.

81. Zhang, Y.; Wang, G.; Wang, L.; Tang, L.; Zhu, M.; Wu, C.; Dou, S.-X.; Wu, M. Graphene-Encapsulated CuP₂: A Promising Anode Material with High Reversible Capacity and Superior Rate-Performance for Sodium-Ion Batteries. *Nano Lett.* **2019**, *19*, 2575–2582. https://doi.org/10.1021/acs.nanolett.9b00342.

82. Liang, S.; Cheng, Y.-J.; Zhu, J.; Xia, Y.; Müller-Buschbaum, P. A Chronicle Review of Nonsilicon (Sn, Sb, Ge)-Based Lithium/Sodium-Ion Battery Alloying Anodes. *Small Methods* **2020**, *4*, 2000218. https://doi.org/10.1002/smtd.202000218.

83. Baggetto, L.; Ganesh, P.; Sun, C.-N.; Meisner, R.A.; Zawodzinski, T.A.; Veith, G.M. Intrinsic thermodynamic and kinetic properties of Sb electrodes for Li-ion and Na-ion batteries: Experiment and theory. *J. Mater. Chem. A* **2013**, *1*, 7985–7994. https://doi.org/10.1039/C3TA11568B.

84. Baggetto, L.; Carroll, K.J.; Hah, H.-Y.; Johnson, C.E.; Mullins, D.R.; Unocic, R.R.; Johnson, J.A.; Meng, Y.S.; Veith, G.M. Probing the Mechanism of Sodium Ion Insertion into Copper Antimony Cu_2Sb Anodes. *J. Phys. Chem. C* **2014**, *118*, 7856–7864. https://doi.org/10.1021/jp501032d.

85. Nie, A.; Gan, L.-Y.; Cheng, Y.; Tao, X.; Yuan, Y.; Sharifi-Asl, S.; He, K.; Asayesh-Ardakani, H.; Vasiraju, V.; Lu, J.; et al. Ultrafast and Highly Reversible Sodium Storage in Zinc-Antimony Intermetallic Nanomaterials. *Adv. Funct. Mater.* **2016**, *26*, 543–552. https://doi.org/10.1002/adfm.201504461.

86. Ji, L.; Gu, M.; Shao, Y.; Li, X.; Engelhard, M.H.; Arey, B.W.; Wang, W.; Nie, Z.; Xiao, J.; Wang, C.; et al. Controlling SEI Formation on SnSb-Porous Carbon Nanofibers for Improved Na Ion Storage. *Adv. Mater.* **2014**, *26*, 2901–2908. https://doi.org/10.1002/adma.201304962.

87. Gao, H.; Wang, Y.; Guo, Z.; Yu, B.; Cheng, G.; Yang, W.; Zhang, Z. Dealloying-induced dual-scale nanoporous indium-antimony anode for sodium/potassium ion batteries. *J. Energy Chem.* **2022**, *75*, 154–163. https://doi.org/10.1016/j.jechem.2022.08.016.

88. Edison, E.; Sreejith, S.; Madhavi, S. Melt-Spun Fe–Sb Intermetallic Alloy Anode for Performance Enhanced Sodium-Ion Batteries. *ACS Appl. Mater. Interfaces* **2017**, *9*, 39399–39406. https://doi.org/10.1021/acsami.7b13096.

89. Baggetto, L.; Allcorn, E.; Unocic, R.R.; Manthiram, A.; Veith, G.M. Mo3Sb7 as a very fast anode material for lithium-ion and sodium-ion batteries. *J. Mater. Chem. A* **2013**, *1*, 11163–11169. https://doi.org/10.1039/C3TA12040F.

90. Zhang, M.; Li, Y.; Wu, F.; Bai, Y.; Wu, C. Boost sodium-ion batteries to commercialization: Strategies to enhance initial Coulombic efficiency of hard carbon anode. *Nano Energy* **2021**, *82*, 105738. https://doi.org/10.1016/j.nanoen.2020.105738.

91. Wang, P.; Zhao, B.; Bai, J.; Tong, P.; Zhu, X.; Sun, Y. Transition Metal Nitrides in Lithium- and Sodium-Ion Batteries: Recent Progress and Perspectives. *Adv. Mater. Interfaces* **2022**, *9*, 2200606. https://doi.org/10.1002/admi.202200606.

92. Liu, K.; Yang, S.; Luo, L.; Pan, Q.; Zhang, P.; Huang, Y.; Zheng, F.; Wang, H.; Li, Q. From spent graphite to recycle graphite anode for high-performance lithium ion batteries and sodium ion batteries. *Electrochim. Acta* **2020**, *356*, 136856. https://doi.org/10.1016/j.electacta.2020.136856.

93. Li, P.; Kim, H.; Myung, S.-T.; Sun, Y.-K. Diverting Exploration of Silicon Anode into Practical Way: A Review Focused on Silicon-Graphite Composite for Lithium Ion Batteries. *Energy Storage Mater.* **2021**, *35*, 550–576. https://doi.org/10.1016/j.ensm.2020.11.028.

94. Wang, Y.; Shi, H.; Niu, J.; Mai, W.; Liu, L.; Xu, Z. Self-healing Sn4P3@Hard carbon Co-storage anode for sodium-ion batteries. *J. Alloys Compd.* **2021**, *851*, 156746. https://doi.org/10.1016/j.jallcom.2020.156746.

95. Cheng, H.; Garcia-Araez, N.; Hector, A.L. Synthesis of Vanadium Nitride–Hard Carbon Composites from Cellulose and Their Performance for Sodium-Ion Batteries. *ACS Appl. Energy Mater.* **2020**, *3*, 4286–4294. https://doi.org/10.1021/acsaem.0c00003.

96. Capone, I.; Hurlbutt, K.; Naylor, A.J.; Xiao, A.W.; Pasta, M. Effect of the Particle-Size Distribution on the Electrochemical Performance of a Red Phosphorus–Carbon Composite Anode for Sodium-Ion Batteries. *Energy Fuels* **2019**, *33*, 4651–4658. https://doi.org/10.1021/acs.energyfuels.9b00385.

97. Mogensen, R.; Colbin, S.; Younesi, R. An Attempt to Formulate Non-Carbonate Electrolytes for Sodium-Ion Batteries. *Batter. Supercaps* **2021**, *4*, 791–814. https://doi.org/10.1002/batt.202000252.

98. Patra, J.; Huang, H.-T.; Xue, W.; Wang, C.; Helal, A.S.; Li, J.; Chang, J.-K. Moderately concentrated electrolyte improves solid–electrolyte interphase and sodium storage performance of hard carbon. *Energy Storage Mater.* **2019**, *16*, 146–154. https://doi.org/10.1016/j.ensm.2018.04.022.

99. Rakov, D.A.; Chen, F.; Ferdousi, S.A.; Li, H.; Pathirana, T.; Simonov, A.N.; Howlett, P.C.; Atkin, R.; Forsyth, M. Engineering high-energy-density sodium battery anodes for improved cycling with superconcentrated ionic-liquid electrolytes. *Nat. Mater.* **2020**, *19*, 1096–1101. https://doi.org/10.1038/s41563-020-0673-0.

100. Sun, C.; Zhang, H.; Mu, P.; Wang, G.; Luo, C.; Zhang, X.; Gao, C.; Zhou, X.; Cui, G. Covalently Cross-Linked Chemistry of a Three-Dimensional Network Binder at Limited Dosage Enables Practical Si/C Composite Electrode Applications. *ACS Nano* **2024**, *18*, 2475–2484. https://doi.org/10.1021/acsnano.3c11286.

101. Xu, M.; Wei, X.; Yan, Z.; Huang, J.; Wu, S.; Ye, K.-H.; Lin, Z. A Fast Self-Healing Binder for Highly Stable SiO$_x$ Anodes in Lithium-Ion Batteries. *ACS Appl. Mater. Interfaces* **2024**, *16*, 55353–55361. https://doi.org/10.1021/acsami.4c11153.

102. Li, R.-R.; Yang, Z.; He, X.-X.; Liu, X.-H.; Zhang, H.; Gao, Y.; Qiao, Y.; Li, L.; Chou, S.-L. Binders for sodium-ion batteries: Progress, challenges and strategies. *Chem. Commun.* **2021**, *57*, 12406–12416. https://doi.org/10.1039/D1CC04563F.

103. Liu, S.; Liu, J.; Wang, W.; Yang, L.; Zhu, K.; Wang, H. Synthesis of coral-like $Fe_2N@C$ nanoparticles and application in sodium ion batteries as a novel anode electrode material. *RSC Adv.* **2016**, *6*, 86131–86136. https://doi.org/10.1039/C6RA17251B.

104. Wang, C.-Y.; Yi, Y.-H.; Chang, W.-C.; Kao, T.-L.; Tuan, H.-Y. Multi-walled carbon nanotube-wrapped SiP_2 as a superior anode material for lithium-ion and sodium-ion batteries. *J. Power Sources* **2018**, *399*, 49–58. https://doi.org/10.1016/j.jpowsour.2018.07.003.

105. Zhao, W.; Ma, X.; Wang, G.; Long, X.; Li, Y.; Zhang, W.; Zhang, P. Carbon-coated CoP_3 nanocomposites as anode materials for high-performance sodium-ion batteries. *Appl. Surf. Sci.* **2018**, *445*, 167–174. https://doi.org/10.1016/j.apsusc.2018.03.126.

106. Hwang, I.-S.; Lee, Y.-H.; Yoon, J.-M.; Hwa, Y.; Park, C.-M. GaSb nanocomposite: New high-performance anode material for Na- and K-ion batteries. *Compos. Part B Eng.* **2022**, *243*, 110142. https://doi.org/10.1016/j.compositesb.2022.110142.

107. Liu, J.; Yang, Z.; Wang, J.; Gu, L.; Maier, J.; Yu, Y. Three-dimensionally interconnected nickel–antimony intermetallic hollow nanospheres as anode material for high-rate sodium-ion batteries. *Nano Energy* **2015**, *16*, 389–398. https://doi.org/10.1016/j.nanoen.2015.07.020.